This article has been accepted for publication in IEEE Journal of Selected Topics in Applied Earth Observations and Remote Sensing. This is the author's version which has not been fully edited and content may change prior to final publication. Citation information: DOI 10.1109/JSTARS.2026.3715093

Comprehensive Evaluation of the CYGNSS V3.2 Soil Moisture Product

Dinan Bai, *Member, IEEE*, Anthony Russel, and Christopher Ruf, *Life Fellow, IEEE*

***Abstract*—The Cyclone Global Navigation Satellite System (CYGNSS) mission offers a novel capability for global soil moisture (SM) monitoring using spaceborne GNSS reflectometry with high temporal revisit and all-weather observation capability. This study presents a comprehensive evaluation of the CYGNSS V3.2 SM product over a seven-year record (Aug 2018 – Dec 2024). The contributions are: (i) an end-to-end evaluation of the V3.2 SM product against SMAP, ISMN in-situ networks, and its legacy V1.0 product using statistical metrics and Triple Collocation; ii) a quantitative linkage between specific Level-0/Level-1 engineering calibration upgrades and measurable improvements in Level-3 SM accuracy and temporal stability; (iii) a seven-year characterization of how retrieval performance is jointly impacted by land-surface homogeneity, inland waterbody, and vegetation phenology; and (iv) a temporal split-sample diagnostic tool to evaluate retrieval stability, identifying retrieval limitations in regimes with sparse training data, weak reflectivity/SM sensitivity, and limited moisture dynamic range. These findings highlight both the advances achieved with CYGNSS V3.2 and the inherent challenges shared by all SM retrievals based on spaceborne GNSS-R systems. They also provide insight into future potential improvements such as dynamic water masking, vegetation-aware modeling, and split-sample stability diagnostics for the next-generation retrieval algorithms.**

***Index Terms*—Soil Moisture, Remote Sensing, GNSS-R, CYGNSS, SMAP, Validation**

I. INTRODUCTION

Near-surface (0-5cm) soil moisture (SM) is a critical component of Earth's hydrological and geophysical processes. It influences energy exchange at the land–atmosphere boundary and serves as a key link between the water, carbon, and energy cycles [1]. Accurate measurement of surface SM and its spatiotemporal variability is essential for hydrological modeling [2], weather forecasting [3], disaster monitoring—including droughts and floods [4], [5], and for supporting agricultural practices, such as irrigation management and crop yield prediction [6]. Consequently, there is a strong need for cost-effective and routine global SM observations. This need can be addressed by spaceborne remote sensing systems, which provide surface SM measurements across a range of spatial and temporal scales. Among them, microwave sensors are commonly used due to their ability to penetrate clouds, vegetation, and the surface soil layer, as well as their strong sensitivity to changes in the soil's dielectric constant caused by moisture [7].

Traditional microwave remote sensing systems, particularly L-band (1–2 GHz) radiometers such as NASA's Soil Moisture Active and Passive (SMAP) mission [8] and ESA's Soil Moisture and Ocean Salinity (SMOS) mission [9], and radars including JAXA's Advanced Land Observing Satellite (ALOS) mission [10], have been widely used for surface SM measurements over the past decades. A promising alternative is Global Navigation Satellite System Reflectometry (GNSS-R), which measures opportunistic L-band GNSS signals scattered from Earth's surface in a bistatic radar configuration [11]. Initially applied to ocean remote sensing, spaceborne GNSS-R was first demonstrated in proof-of-concept missions such as UK-DMC (2004) [12] and TDS-1 (2014) [13]. NASA's Cyclone Global Navigation Satellite System (CYGNSS), launched in 2016, was originally designed to measure ocean surface wind speeds within tropical cyclones to improve storm forecasts [14], [15], using a constellation of eight smallsats. Later, its scope expanded to terrestrial remote sensing, driven by studies [16], [17], [18] showing the sensitivity of GNSS-R to land surface reflectivity, a parameter closely linked to surface SM. The CYGNSS constellation enables rapid revisit at daily and sub-daily (6-hour) intervals, allowing for monitoring of rapidly evolving hydrological events and diurnal soil moisture changes, supporting a wide range of valuable scientific applications [19].

Early study [20] demonstrated strong correlations between CYGNSS-measured surface reflectivity and SMAP soil moisture and led to the first global CYGNSS Level-3 (L3) soil moisture product (Version 1.0), based on a linear regression between CYGNSS Level-1 (L1) effective reflectivity and SMAP soil moisture. Since then, CYGNSS data have supported a variety of empirical [21], [22], [23], physical [24], [25], and machine-learning [26], [27], [28] based SM retrieval approaches, and the V1.0 product has become a common reference for intercomparison with these CYGNSS SM products and other recently launched GNSS-R missions such as Spire [29], MuSat [30], Fengyun-3 [31], and Tianmu-1 [32], most of which adopt retrieval algorithms based on the same regression-type empirical modeling framework.

The quality of any GNSS-R SM retrieval fundamentally depends on the accuracy and stability of its Level-1 reflectivity calibration. In CYGNSS, the newly released V3.2 L1 dataset incorporates several major updates, including dynamic transmitter power (EIRP) correction [33], refined Delay Doppler map (DDM) noise-floor estimation [34], and compensation for temperature-dependent receiver effects [35]. These updates significantly improve the consistency and physical accuracy of land surface reflectivity retrievals, thereby enabling a new generation of CYGNSS SM products. The corresponding Level-3 product (CYGNSS SM V3.2) uses the recalibrated L1 inputs, allowing a direct comparison with earlier versions and an assessment of the impact of calibration improvements on SM performance.

This work is licensed under a Creative Commons Attribution 4.0 License. For more information, see https://creativecommons.org/licenses/by/4.0/

This article has been accepted for publication in IEEE Journal of Selected Topics in Applied Earth Observations and Remote Sensing. This is the author's version which has not been fully edited, content may change prior to final publication. Citation information: DOI 10.1109/JSTARS.2026.3715093

This study presents a comprehensive performance assessment of the CYGNSS V3.2 SM product. Leveraging seven years of continuous global CYGNSS observations, the study characterizes the long-term spatial and temporal behavior of GNSS-R SM retrievals across diverse land-cover and climatic regimes. First, we conduct an end-to-end evaluation of the V3.2 SM product against SMAP, ISMN in-situ networks, and its legacy V1.0 product, complementing cross-product consistency assessment with independent in-situ validation and Triple Collocation. Second, we provide a quantitative linkage between the specific Level-0/Level-1 Engineering Calibration upgrades introduced in V3.2 as described above and the measurable improvements they produce in the Level-3 SM product. Third, we use the full seven-year record to characterize how retrieval performance is shaped by land-surface homogeneity, inland-water body, and vegetation phenology in spatial and temporal scales. Fourth, we adapt temporal split-sample cross-validation to the per-grid-cell level SM retrieval to analyze the model stability, providing insights into where and why GNSS-R empirical retrievals degrade. Because many existing GNSS-R SM products, including those from CYGNSS and emerging GNSS-R constellations, rely on similar empirical formulations, the insights gained here extend beyond CYGNSS itself. The results provide a benchmark for future GNSS-R SM retrieval algorithm development, inform the fusion of SM products across single and multiple GNSS-R missions [36], and support the integration of CYGNSS SM data into SM assimilation systems.

This paper is organized as follows: Section II describes the soil moisture datasets used for performance validation; Section III outlines the retrieval methodology and evaluation metrics; Section IV and V present the performance characterization results; Section VI summarizes the key findings and discusses their implications for future retrieval model improvements; and Section VII concludes the study.

II. Soil Moisture and Ancillary Datasets

We first describe the CYGNSS V3.2 SM product and briefly summarize its development. We then introduce reference and ancillary datasets used for evaluation.

A. CYGNSS V3.2 Soil Moisture Product

CYGNSS is an eight-satellite constellation that measures bistatic scattering of GNSS L-band signals, providing coverage between 38° S and 38° N latitude with a mean revisit of ~7 h [37]. Under fully coherent conditions [38], the nominal footprint is ~7 km along-track × 0.5 km cross-track; after July 2019, shortening the incoherent integration time from 1.0 s to 0.5 s reduced the along-track dimension to ~3.5 km. The L1 Science Data Record contains calibrated delay–Doppler measurements. The latest release, V3.2 (Aug 2018–present), introduces a refined DDM noise-floor correction [34], compensation for temperature-dependent receiver variations [35], and dynamic EIRP estimation for GPS transmitters [33], along with expanded quality flags, together yielding a more accurate, precise and stable land reflectivity product.

The CYGNSS L3 SM V3.2 product is derived from this recalibrated L1 dataset. Combined with the empirical GNSS-R retrieval summarized in Section II B, it provides global near-surface (0–5 cm) SM at 9 km and 36 km resolution on the EASE-Grid 2.0, with daily (24 h) and sub-daily (6 h) averages across the ±38° latitude range observed by CYGNSS.

B. Soil Moisture Retrieval with GNSS-R

The CYGNSS SM retrieval is based on the sensitivity of surface effective reflectivity Γ_{eff} to changes in the soil dielectric constant, which depends primarily on volumetric water content [39]. CYGNSS measures the power of L-band GNSS signals reflected from Earth's surface in the form of a Delay Doppler Map (DDM) [37]. For each reflection, the DDM peak power P_r is converted to a surface effective reflectivity Γ_{eff} through:

$$\Gamma_{\text{eff}} = \frac{(4\pi)^2}{\lambda^2} \cdot \frac{(R_T + R_R)^2}{EIRP \cdot G_R} \cdot P_r \quad (1)$$

where λ represents the GNSS wavelength ($\approx 19\ cm$); R_T and R_R are the distances from the transmitter and receiver to the specular point, respectively; EIRP (Equivalent Isotropic Radiated Power) is the product of the transmitter antenna gain and transmitted power of GNSS satellites; and G_R is the CYGNSS receiver's antenna gain in the specular direction. The effective reflectivity represents the combined influence of surface dielectric properties, roughness, and vegetation attenuation [40]:

$$\Gamma_{\text{eff}} = \Gamma_{soil}(\epsilon, \theta_i) \cdot \gamma_{RN} \cdot \gamma_{VG} \quad (2)$$

where Γ_{soil} is the Fresnel Reflectivity of the soil surface, ϵ is the permittivity of the surface, θ_i is the incidence angle, and γ_{RN} and γ_{VG} are attenuation terms due to surface roughness and vegetation, respectively. The roughness term γ_{RN} is expressed as:

$$\gamma_{RN} = \exp(-4k_0^2 h^2 \cos(\theta_i)^2) \quad (3)$$

where the electromagnetic wave number $k_0 = 2\pi/\lambda$, and h is the surface root-mean-square (RMS) height, which characterizes the roughness of the local surface. The vegetation term γ_{VG} is expressed as:

$$\gamma_{VG} = \exp(-2\tau_v \sec(\theta_i)) \quad (4)$$

where τ_v represents the vegetation optical depth (VOD).

For all current spaceborne GNSS-R systems, retrieval of soil moisture from Γ_{eff} is inherently under-constrained because several surface parameters, including soil permittivity, roughness, and vegetation attenuation, jointly affect the measured signal and their effects cannot be separated using only GNSS-R observables. Existing ancillary datasets typically lack the spatial resolution and temporal variability necessary to accurately represent the electromagnetic scattering parameters in the GNSS-R forward model. Consequently, most GNSS-R SM retrievals adopt empirical approaches, primarily belonging to regression-based [20], [23], [29] and machine-learning [26], [41] families, in which measured reflectivity is directly related to reference SM data. These methods capture the dominant sensitivity of Γ_{eff} to dielectric changes in the soil while statistically incorporating vegetation (e.g. τ_v) and terrain effects (e.g. h, soil texture) through its empirical model coefficients. Such empirical formulations have been widely adopted across GNSS-R missions and have demonstrated generally good retrieval performance, yet further investigations are still

This work is licensed under a Creative Commons Attribution 4.0 License. For more information, see https://creativecommons.org/licenses/by/4.0/

This article has been accepted for publication in IEEE Journal of Selected Topics in Applied Earth Observations and Remote Sensing. This is the author's version which has not been fully edited content may change prior to final publication. Citation information: DOI 10.1109/JSTARS.2026.3715093

required to understand their long-term spatial and temporal behavior across diverse land-cover and climate regimes.

The CYGNSS SM product empirically relates the effective reflectivity Γ_{eff} to coincident and collocated SMAP SM observations using a linear regression of the form

$$SM = \beta \cdot \Gamma_{\text{eff}} + \alpha \quad (5)$$

where α and β are the intercept and slope coefficients determined within local 3 km sub-cells of the 36 km EASE-Grid, a size that is comparable to the CYGNSS footprint size under coherent condition. The trained coefficients are then applied to all valid CYGNSS reflectivity measurements to upscale to 9 and 36 km to generate daily and sub-daily SM products. This empirical model formulation has been the operational approach for CYGNSS SM retrievals and is described in detail in the CYGNSS Level 3 Algorithm Theoretical Basis Document [42]. Further algorithmic details, including training procedures and quality-control flags, are provided in that document and are not repeated here.

C. Reference and Ancillary Datasets

1) **CYGNSS Level-3 Soil Moisture V1.0:** The first CYGNSS SM product [20], provides 0–5 cm surface SM estimates between 38° S and 38° N at daily and 6-hour intervals from March 2017 to June 2024. For the V1.0–V3.2 comparisons reported in this study, the CYGNSS Science Operations Center applied the legacy V1.0 retrieval model to extend the V1.0 SM product through 31 December 2024, although this extended portion is not part of the publicly released V1.0 product. The retrieval uses an empirical linear regression between CYGNSS Level-1 effective reflectivity and collocated SMAP Level-3 SM, trained and applied using L1 V2.1 data. Comparisons to V1.0 are included here to benchmark the improvements introduced in V3.2.
2) **SMAP Soil Moisture**: SMAP measures near-surface (0–5 cm) SM using an L-band radiometer at 6 a.m. and 6 p.m. local time with 2–3-day revisit. We use Level-3 Radiometer Global Daily products at 9 km and 36 km resolution [43], [44], from 1 August 2018 to 31 December 2024. Descending-orbit Dual-Channel Algorithm (DCA) retrievals are selected to minimize thermal-diurnal effects. The 'SM successful retrieval' quality flag is applied. SMAP L3 vegetation optical depth (VOD) is obtained from the same DCA retrieval used for the SMAP SM product.
3) **ESA CCI Active Soil Moisture**: The ESA Climate Change Initiative (CCI) Active SM product (Version 09.2) merges scatterometer based SM retrievals, primarily from the MetOp Advanced Scatterometer (ASCAT) [45] . The dataset provides daily global coverage from 1 August 2018 to 31 December 2024 at 0.25° resolution (≈ 28 km at the equator). Data are projected onto the 36 km EASE-Grid 2.0 to align with CYGNSS and SMAP grids.
4) **ISMN Soil Moisture**: In-situ SM observations are obtained from the International Soil Moisture Network (ISMN) [46], including eight networks: ARM [47], OZNET [48], SCAN [49], SNOTEL [50], SoilSCAPE [51], USCRN [52], TAHMO [53], and TxSON [54] with 288 stations. Only high-quality top-layer (0–5 cm) measurements are used. Hourly data are averaged to daily means for consistency with satellite products. Fig. 1 shows the spatial distribution of all ISMN stations.
5) **Ancillary Data**: Land cover classification is used in this study to characterize soil moisture retrieval performance across different land surface types. We use the 17-class International Geosphere–Biosphere Program (IGBP) land cover classification dataset (MCD12C1, Version 061) from the year 2022 [55]. The global land cover map is shown in Fig. 1. For each 36 km EASE grid cell, the dominant land cover type is identified, and the fraction of the dominant class is computed to quantify the degree of surface homogeneity. For each ISMN station, IGBP land cover types are grouped into six major categories, as summarized in Table 1. A single-year (2022) IGBP land cover classification is used for stratification across the full study period. While major land cover

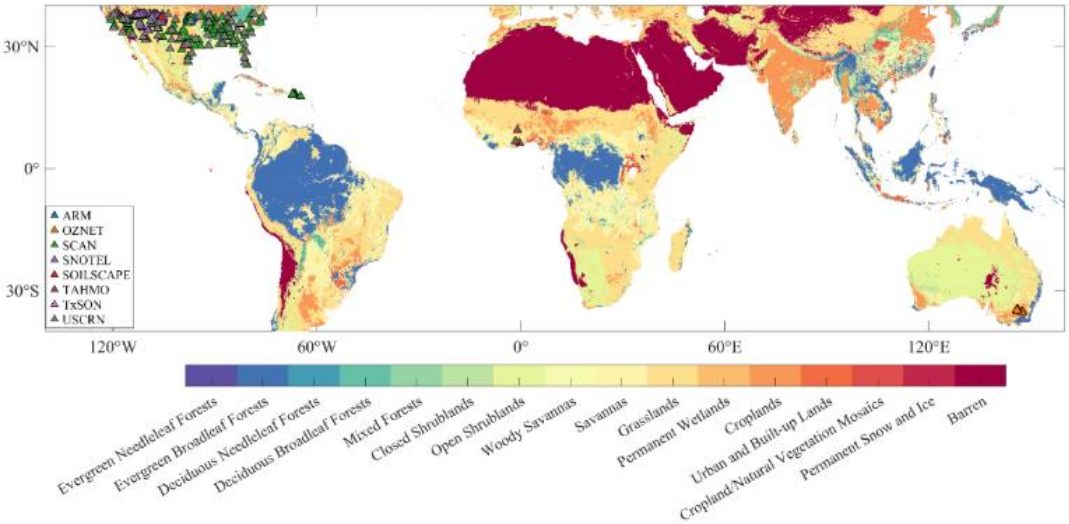


Fig. 1. The spatial distribution of eight selected ISMN networks overlaid on a $0.05 \times 0.05°$ IGBP land classification map (MCD12C1 2023).

This work is licensed under a Creative Commons Attribution 4.0 License. For more information, see https://creativecommons.org/licenses/by/4.0/

This article has been accepted for publication in IEEE Journal of Selected Topics in Applied Earth Observations and Remote Sensing. This is the author's version which has not been fully edited, content may change prior to final publication. Citation information: DOI 10.1109/JSTARS.2026.3715093

types are relatively stable at 36 km resolution over 7 years, we acknowledge that land cover changes (e.g., deforestation, urbanization) are not captured, which may introduce minor inaccuracies in the stratified analysis.

Table 1. IGBP Land Classification and ISMN stations associated with each class

IGBP Class	Land Classification	Major Type	# of Station
1	Evergreen Needleleaf Forests	Forest	13
2	Evergreen Broadleaf Forests		
3	Deciduous Needleleaf Forests		
4	Deciduous Broadleaf Forests		
5	Mixed Forests		
6	Closed Shrublands	Shrubland	26
7	Open Shrublands		
8	Woody Savannas	Savanna	65
9	Savannas		
10	Grasslands	Grassland	115
12	Croplands	Cropland	59
14	Cropland/Natural Vegetation Mosaics		
13	Urban and Built-up Lands	Barren	10
16	Barren		
15	Permanent Snow and Ice		
0	Water Body	/	
11	Permanent Wetlands		

III. Evaluation Methodology

A. Statistical Metrics

Let x denote the reference SM and y the corresponding value of the product being evaluated. We compute the standard metrics—root-mean-square difference (RMSD), bias b, unbiased RMSD (ubRMSD), and Pearson correlation r, on collocated pairs $\{(x_i, y_i)\}_{i=1}^{N}$:

$$RMSD = \sqrt{\frac{1}{N}\sum_{i=1}^{N}(y_i - x_i)^2} \tag{6}$$

$$b = \frac{1}{N}\sum_{i=1}^{N} y_i - x_i \tag{7}$$

$$ubRMSD = \sqrt{\frac{1}{N}\sum_{i=1}^{N}[(y_i - \overline{y_i}) - (x_i - \overline{x_i})]^2} \tag{8}$$

$$R = \frac{cov(x,y)}{\sqrt{var(x)\cdot var(y)}} \tag{9}$$

RMSD quantifies total disagreement (random + systematic); bias b captures the mean offset. When b is time-invariant and (7) is computed using full-series means $\bar{x}, \bar{y}$, the identity $\mathrm{RMSD}^2 = \mathrm{ubRMSD}^2 + b^2$ holds [56]. However, SM datasets often exhibit seasonal bias. To avoid inflating RMSD and correlation by the annual cycle, we remove monthly climatological means prior to computing ubRMSD: for month m, define anomalies $x_i' = x_i - \bar{x}(m)$ and $y_i' = y_i - \bar{y}(m)$, and compute ubRMSD on (x_i', y_i'). Under this deseasonalized treatment, the RMSD–ubRMSD–bias identity need not hold over the full multi-year record. Pearson correlation r gauges phase (timing) agreement between the retrieved and reference SM. However over long records dominated by the seasonal cycle, r can appear spuriously high even when short-term variability is poorly captured.

In this study, the reference SM is drawn from two datasets: the SMAP L3 SM product and ISMN in-situ observations. SMAP itself achieves strong global performance and remains a valuable reference for characterizing how CYGNSS performs and how its consistency with SMAP varies across diverse environments and climate regimes, and for tracking the inter-product improvement from V1.0 to V3.2. We note, however, that in regions where SMAP itself performs poorly, the trained CYGNSS regression inherits the same limitations, and the two products might disagree with the truth in similar ways. Independent accuracy is therefore assessed against ISMN (Section IV C) and complemented by the Triple Collocation analysis introduced in Section III B and applied in Section IV I.

B. Triple Collocation

While the standard evaluation metrics in Section III A rely on one SM dataset as the reference, the reference, often derived from another measurement system, still carries its own errors and thus differs from the 'ground truth' of SM. The Triple Collocation (TC) algorithm [57] addresses this by using three mutually independent measurement systems to estimate the Root Mean Square Error (RMSE) of each of them with respect to the true but unobserved SM. The extended Triple Collocation (ETC) method [58] further allows estimation of the correlation between each dataset and the unknown truth.

TC and ETC are based on the following assumptions: (1) a linear relationship between the true SM and observations; (2) stationarity of errors; (3) errors in the three SM datasets are mutually independent; (4) errors in the three datasets are independent of the ground truth. For three collocated measurement systems x_i, $i \in \{1,2,3\}$, they are linearly related to the true value t by:

$$x_i = \alpha_i + \beta_i t + \epsilon_i \tag{10}$$

where ϵ_i is the zero-mean random error in measurement x_i. With the above assumptions, the covariance between measurements x_i and x_j is given by:

$$Q_{ij} = cov(x_i, x_j) = \begin{cases} \beta_i\beta_j\sigma_t^2, & for\ i \neq j \\ \beta_i^2\sigma_t^2 + \sigma_{\epsilon_i}^2, & for\ i = j \end{cases} \tag{11}$$

Where $\sigma_t^2 = var(t)$ and $\sigma_{\epsilon_i}^2 = var(\epsilon_i)$. By defining $\theta_i = \beta_i\sigma_t$, we get:

$$Q_{ij} = \begin{cases} \theta_i\theta_j, & for\ i \neq j \\ \theta_i^2 + \sigma_{\epsilon_i}^2, & for\ i = j \end{cases} \tag{12}$$

With six unknowns (θ_i and σ_{ϵ_i}) and six equations ($Q_{11}, Q_{22}, Q_{33}, Q_{12}, Q_{13}, Q_{23}$), the RMSE can be solved:

This work is licensed under a Creative Commons Attribution 4.0 License. For more information, see https://creativecommons.org/licenses/by/4.0/

This article has been accepted for publication in IEEE Journal of Selected Topics in Applied Earth Observations and Remote Sensing. This is the author's version which has not been fully edited and content may change prior to final publication. Citation information: DOI 10.1109/JSTARS.2026.3715093

$$RMSE = \left[\sqrt{Q_{11} - \frac{Q_{12}Q_{13}}{Q_{23}}} \quad \sqrt{Q_{22} - \frac{Q_{12}Q_{23}}{Q_{13}}} \quad \sqrt{Q_{33} - \frac{Q_{13}Q_{23}}{Q_{12}}}\right]^T \quad (13)$$

and the correlation is given by:

$$r = \left[\sqrt{\frac{Q_{12}Q_{13}}{Q_{11}Q_{23}}} \quad \sqrt{\frac{Q_{12}Q_{23}}{Q_{22}Q_{13}}} \quad \sqrt{\frac{Q_{13}Q_{23}}{Q_{33}Q_{12}}}\right]^T \quad (14)$$

To reduce spurious cross-correlation from shared seasonality, TC/ETC are applied to monthly anomaly series (each product's monthly climatology removed) before computing covariances.

In Section IV I, TC triplets are formed using subsets of the {CYGNSS/SMAP, ESA CCI Active, ISMN in-situ} datasets. Since the CYGNSS SM retrieval is trained directly against SMAP as the reference, their errors are inherently correlated. To avoid violating ETC assumptions, CYGNSS and SMAP are placed in separate triplets. The use of ESA CCI Active as the third member of each triplet removes by design any shared instrument between the triplet members: the CCI Active product is built from active microwave scatterometer retrievals and contributes no observation in common with either SMAP or CYGNSS. The SMAP/ASCAT/in-situ triplet and equivalent scatterometer/passive/in-situ configurations have been used extensively in prior SM TC studies [59], [60], in which the residual SMAP–ASCAT error cross-correlation in those studies has been estimated at a median of about 0.19, within the range typically considered acceptable for TC/ETC analysis [61]. ISMN in-situ observations are likewise treated as an independent reference here and in prior work [59], [60]: the SMAP DCA retrieval is a physics-based radiative-transfer inversion that does not ingest ISMN data, so any SMAP–ISMN error correlation is expected to be weak, consistent with the broader community of SMAP validation studies that adopt ISMN as an independent reference.

We acknowledge that none of these inter-dataset error correlations are strictly zero, and note that any residual positive correlation can in principle act to slightly inflate the TC-derived correlation with the latent truth and slightly depress the TC-derived RMSE [61]. The TC results in Section IV I are therefore presented as a complementary line of evidence alongside the direct SMAP cross-product comparisons (Sections IV B, IV D, IV E) and the independent ISMN validation (Section IV C), rather than as a standalone measure of absolute retrieval truth. A detailed sensitivity treatment of residual error correlation is available in the cited TC literature.

C. Performance Evaluation Framework

This section outlines how we use the metrics in Section III A and the TC/ETC formulation in Section III B to assess CYGNSS SM performance across spatial, temporal, and environmental dimensions with the following frameworks:

1) Overall performance: We provide an overview of the SM product spatiotemporal resolution and an overall performance assessment of CYGNSS SM against SMAP and ISMN reference datasets. The comparison uses standard statistical metrics to characterize agreement across different spatial resolutions and independent observation sources.
2) Temporal performance analysis: We analyze seven years of monthly statistical metrics to examine the improvement in long-term consistency introduced by the V3.2 Level-1 calibration. Seasonal amplitude and phase variations in these metrics are interpreted with respect to vegetation phenology, providing physical context for observed temporal patterns. The impact of inland water bodies on long-term SM retrieval quality is also examined.
3) Spatial performance analysis: We evaluate statistical metrics grouped by IGBP land-cover class to characterize how retrieval performance varies with surface type. This stratified analysis highlights the influence of land-cover heterogeneity, inland waterbodies, and vegetation on CYGNSS SM performance.
4) Triple Collocation assessment: We apply TC using the triplets {CYGNSS, ISMN, ESA CCI Active} and {SMAP, ISMN, ESA CCI Active} over the same ISMN stations, land-cover groups, and evaluation period to estimate the correlation and RMSE of the CYGNSS and SMAP SM products relative to the true SM state. Results are reported as land cover group statistics, providing an independent benchmark of product accuracy.
5) Model stability diagnosis: We observe degraded performance when transitioning from training to testing periods, indicative of the robustness of empirical GNSS-R SM models. This analysis is used to illustrate the underlying challenges in model stability, which are further discussed in Section V.

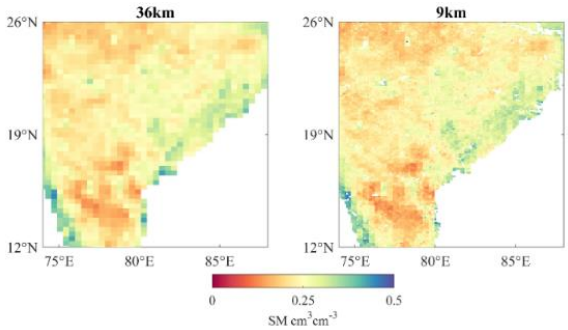


Fig. 2. Spatial resolution comparison of CYGNSS V3.2 36 (left) and 9 km (right) SM products in the area of 74°E to 88°E and 12°N to 26°N. SM obtained between 2018 Oct and Nov are averaged per grid.

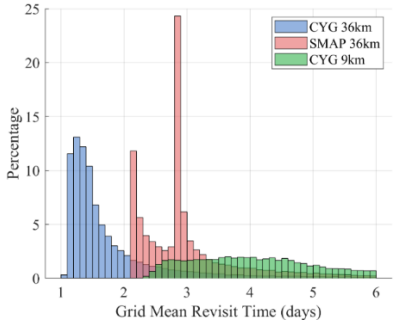


Fig. 3. Histograms of mean revisit time per grid of CYGNSS 36 km, 9 km, and SMAP 36 km SM daily products.

This work is licensed under a Creative Commons Attribution 4.0 License. For more information, see https://creativecommons.org/licenses/by/4.0/

This article has been accepted for publication in IEEE Journal of Selected Topics in Applied Earth Observations and Remote Sensing. This is the author's version which has not been fully edited and content may change prior to final publication. Citation information: DOI 10.1109/JSTARS.2026.3715093

IV. Performance Characterization Results

A. Overall Spatial and Temporal Pattern

The CYGNSS V3.2 soil moisture product is available at both 9 km and 36 km spatial resolutions. Fig. 2 compares the two resolutions using soil moisture data collected during October and November 2018 over a portion of the Indian subcontinent. The 9 km product reveals finer spatial details in soil moisture patterns compared to the coarser 36 km version, reflecting the benefit of higher-resolution retrieval based on subcell-scale information.

The CYGNSS constellation's rapid revisit capability distinguishes it from single-satellite missions. Fig. 3 shows the distribution of effective revisit times per grid cell within ±38° latitude for CYGNSS 9 and 36 km and SMAP 36 km SM products. CYGNSS 36 km provides the most frequent sampling, with a median revisit time of approximately 1.3 days. In contrast, the SMAP 36 km product shows a bimodal distribution, with peaks at approximately 2.15 and 2.85 days, corresponding to its orbital pattern across low and high latitudes. The SMAP 9 km product is derived from 36 km radiometer data [62] and thus has a similar revisit time, so it is omitted. The CYGNSS 9 km product achieves finer spatial detail at the cost of a longer revisit time (median ≈ 5.7 days) and a large variance across grid cells (values beyond 6 days are clipped in the plot). This trade-off between spatial resolution and temporal coverage is a feature that is common to most CYGNSS products [63].

B. Overall Performance against SMAP

For the 36 km resolution products, CYGNSS and SMAP exhibit a strong correlation of 0.92 (95% confidence interval [0.91, 0.93]) and an RMSD of 0.049 $cm^3\ cm^{-3}$ (95% confidence interval [0.048, 0.049]). For the 9 km products, the correlation is 0.89 (95% confidence interval [0.88, 0.89]) with an RMSD of 0.052 $cm^3\ cm^{-3}$ (95% confidence interval [0.051, 0.052]). Fig. 4 presents global maps of correlation and RMSD between CYGNSS and SMAP SM for the period from August 2018 to December 2024. Panels (a) and (b) show the correlation and RMSD, respectively, for the CYGNSS V3.2 36 km product, while panels (c) and (d) display the same metrics for the 9 km product. High correlation values are observed in regions with moderate vegetation and SM variability—such as the South America, Central and South Africa, and eastern and north Australia. In contrast, arid zones, mountain areas, and densely vegetated tropical regions show lower correlation and higher RMSD, reflecting limited dynamic range and reduced sensitivity of GNSS-R signals to SM under those surface conditions.

It is worth noting that the global distribution patterns of correlation R and RMSD in CYGNSS V3.2 are broadly consistent with those reported for earlier CYGNSS SM products and other GNSS-R missions due to the common characteristics of current GNSS-R signal processing techniques and empirical SM retrieval algorithms.

C. Overall Performance against in-situ SM

The overall performance of CYGNSS soil moisture products compared to selected ISMN networks and land covers are summarized in Table S1 and Table S2. For each product, the median values of correlation, bias, RMSD, ubRMSD, and their 95% bias-corrected and accelerated (BCa) bootstrap confidence intervals are reported across all networks. The last two columns of Table S1 and Table S2 report a one-sided paired Wilcoxon signed-rank test of whether the V3.2 product (36 km or 9 km) is significantly better than V1.0 36 km for each ISMN network and land cover. The reported p-values therefore quantify the strength of these improvements: $p<0.001$ indicates strong statistical significance that V3.2 outperforms V1.0 in the corresponding metric, while large p-values (e.g. $p>0.05$) indicate that the improvement is not statistically significant. The V1.0 product serves as the comparison baseline and is marked '-'.

Overall, the V3.2 36 km and 9 km products demonstrate improved performance relative to the V1.0 product. Paired statistics tests at the per-station level confirm that the V3.2 36 km product is significantly better than V1.0 in correlation (median per-station improvement +0.057, 95 % CI [+0.051, +0.063]; one-sided Wilcoxon $p < 0.001$) and ubRMSD (median ΔubRMSD −0.0018 $cm^3\ cm^{-3}$, 95% CI [-0.0024, -0.0014]; $p < 0.001$). The V3.2 9 km product also significantly improves ubRMSD over V1.0 (median ΔubRMSD -0.0011 $cm^3\ cm^{-3}$, 95% CI [-0.0018, -0.0003]; $p < 0.001$) but the gain in correlation is only marginally distinguishable from zero (median +0.013, 95% CI [-0.004, 0.029]; $p = 0.043$).

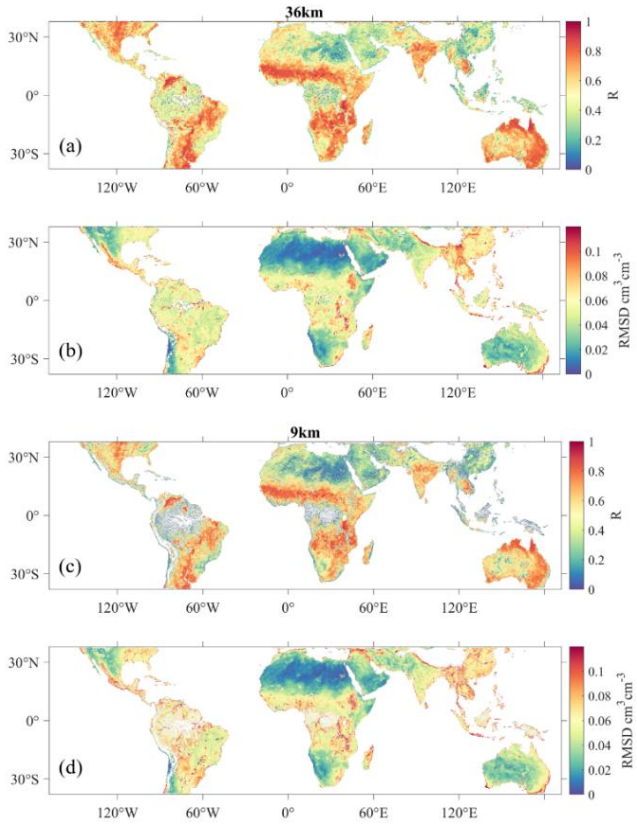


Fig. 4. Global map of (a) Correlation and (b) RMSD per grid between CYGNSS and SMAP 36 km SM products, and (c) Correlation and (d) RMSD per grid between CYGNSS and SMAP 9 km SM products.

This work is licensed under a Creative Commons Attribution 4.0 License. For more information, see https://creativecommons.org/licenses/by/4.0/

This article has been accepted for publication in IEEE Journal of Selected Topics in Applied Earth Observations and Remote Sensing. This is the author's version which has not been fully edited content may change prior to final publication. Citation information: DOI 10.1109/JSTARS.2026.3715093

D. Temporal Performance Analysis

The CYGNSS V1.0 and V3.2 SM products provide over seven years of continuous observations, which enables an assessment of long-term retrieval performance. The length of this record allows for the evaluation of the temporal stability of both the underlying system calibration and the retrieval model.

Fig. 5 presents the monthly global correlation, bias, RMSD, and ubRMSD (with monthly bias removed) between CYGNSS and SMAP SM products from 1 August 2018 to 31 December 2024. Among all versions, the CYGNSS V3.2 36 km product exhibits the best performance, consistently achieving the highest correlation and the lowest RMSD and ubRMSD values over the evaluation period. The V3.2 9 km product follows a similar long-term trend, though with slightly degraded performance. This degradation is expected, as the 9 km product is derived from linear regression models trained at the 3 km subcell level using the coarser SMAP 36 km product as the reference, which introduces additional representativeness error. Both CYGNSS V3.2 products demonstrate significant improvements over the original V1.0 36 km product. These improvements reflect refinements in CYGNSS system calibration introduced in the L1 V3.2 processing, which yield more accurate and consistent surface reflectivity measurements and therefore enhance the quality and temporal stability of the SM retrievals.

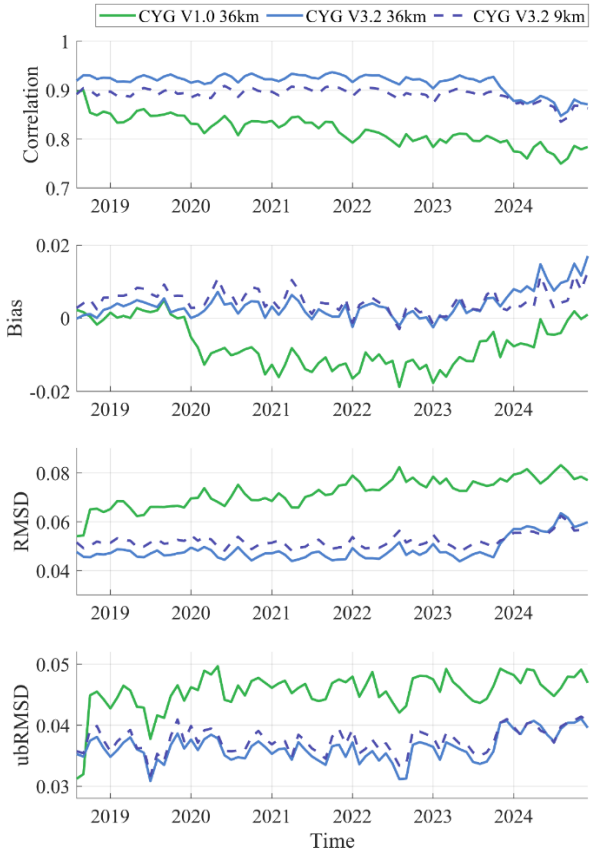


Fig. 5. Monthly correlation, bias, RMSD, ubRMSD between CYGNSS V1.0 36 km SM (green), V3.2 36 km SM (blue), V3.2 9 km SM (dark blue dash) and SMAP 36 km and 9 km SM from 8/1/2018 to 12/31/2024.

In the bias time series shown in Fig. 5, a noticeable negative shift emerges between the CYGNSS V1.0 and SMAP 36 km SM products beginning in early 2020. This discontinuity coincides with the widespread activation of the GPS Flex Power mode, in which newer GPS satellite blocks dynamically redistribute transmit power among signal components over specific geographic regions [33]. The GPS transmit power is characterized by Equivalent Isotropic Radiated Power (EIRP), the product of GPS transmit power and antenna gain. As shown in (1), the surface effective reflectivity is inversely proportional to the EIRP, i.e., $\Gamma_{\mathrm{eff}} \propto 1/EIRP$. Therefore, an overestimation of EIRP leads directly to an underestimation of Γ_{eff} and consequently biases the retrieved SM low.

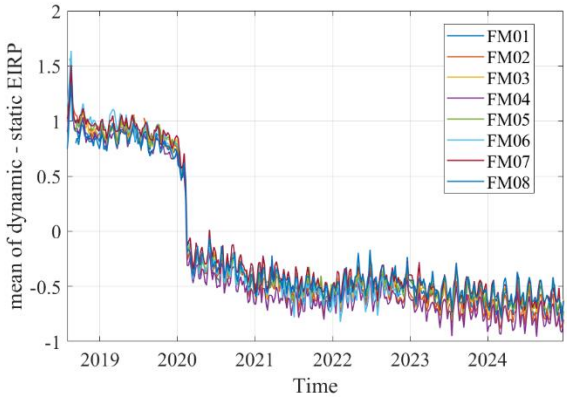


Fig. 6. Global weekly mean bias between CYGNSS L1 dynamic and static EIRP from satellite FM01 to FM08.

To address this issue, the CYGNSS calibration team developed a dynamic Equivalent Isotropic Radiated Power (EIRP) estimation approach that provides real-time measurements of GPS transmit power, and this capability is incorporated into the V3.2 Level-1 calibration [33]. In contrast, the Version 2.1 L1 calibration used in the V1.0 SM product applies a static EIRP assumption, treating GPS transmit power as constant. The static model therefore fails to account for the Flex Power induced reduction in signal power starting in 2020. As shown in Fig. 6, the global weekly mean difference between dynamic and static EIRP estimates from all CYGNSS satellites (FM01–FM08) exhibits a sudden drop of approximately 1.5 dB at the start of 2020. This represents a real reduction in GPS transmitted power that the static model does not capture. As a result, the V1.0 product systematically underestimates Γ_{eff} and soil moisture after 2020.

Although Fig. 6 indicates an approximately constant offset (~1 dB) prior to 2020, this offset had already been absorbed during the V1.0 retrieval model training. As long as the EIRP bias remained temporally stable, its impact on retrieval performance was minimized. However, once the transmit power began varying in time, the static EIRP model became inadequate. Thus, to correctly capture the temporal evolution of Γ_{eff} and soil moisture, the dynamic EIRP estimation must be incorporated into the L1 calibration algorithm, as implemented in V3.2.

In addition to the GPS Flex Power related discontinuity, we observe a gradual upward trend in the monthly global mean bias in Fig. 5 for both V1.0 and V3.2 products beginning in early 2023. Since this trend is absent in CYGNSS ocean observations

This work is licensed under a Creative Commons Attribution 4.0 License. For more information, see https://creativecommons.org/licenses/by/4.0/

This article has been accepted for publication in IEEE Journal of Selected Topics in Applied Earth Observations and Remote Sensing. This is the author's version which has not been fully edited content may change prior to final publication. Citation information: DOI 10.1109/JSTARS.2026.3715093

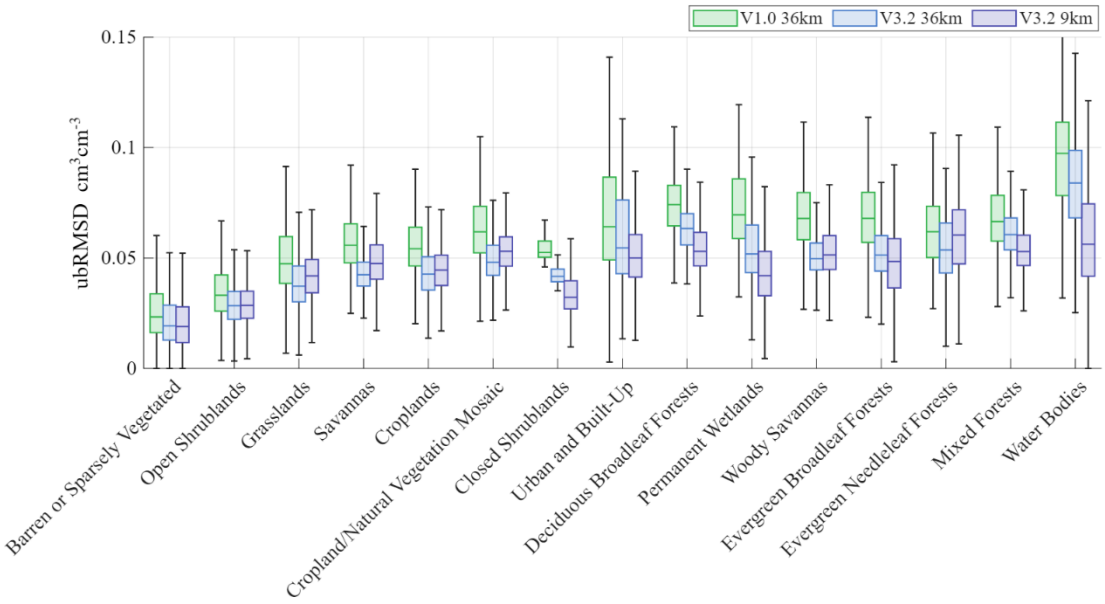


Fig. 7. Retrieval performance (ubRMSD) between CYGNSS and SMAP SM products across IGBP land classes.

[64], which serve as the calibration reference for L1 products, and is common to both product versions, we conclude that it is unlikely to originate from L1 calibration. Instead, our analysis indicates that the bias pattern is consistent with inland waterbody contributions to the measured reflectivity that are only partially represented by the current static water mask and retrieval framework. The influence of inland waterbodies on SM retrievals is examined in detail in Section IV G.

In Fig. 5, we observe a mild performance degradation, shown as decreased correlation and increased RMSD and ubRMSD, for the CYGNSS V3.2 and V1.0 products in November 2023 and October 2018, respectively. These dates correspond to the endpoints of the regression model training periods (15 November 2023, for V3.2 and 1 October 2018, for V1.0). This behavior reflects a degradation in retrieval accuracy when the model is applied outside of the training window. The underlying causes and implications of this behavior for empirical SM retrieval models are examined in Section V.

E. Land Cover Dependence

This subsection examines how the performance of the CYGNSS SM retrieval varies across different IGBP land-cover types. By comparing CYGNSS with SMAP and ISMN reference datasets, we evaluate how land cover influences retrieval accuracy among the different versions of CYGNSS products.

Over seven years of simultaneous operation, CYGNSS and SMAP together provide a dense global record of collocated SM measurements, with thousands of matchups available for each land-cover type. This extensive dataset enables a robust statistical evaluation of retrieval performance. Fig. 7 presents the distribution of ubRMSD for each IGBP land cover type, shown as box plots. In each plot, the central line indicates the median, the box edges represent the interquartile range (25th to 75th percentiles), and the whiskers extend to the 10th and 90th percentiles. The ubRMSD metric isolates short-term retrieval variability by removing the monthly mean bias, providing a clearer measure of random error independent of seasonal effects. Across all land cover types, the CYGNSS V3.2 product shows improved performance compared to V1.0, with particularly notable improvement in vegetated areas, especially forested regions. In addition, the V3.2 9 km product exhibits lower ubRMSD than the 36 km product in forested areas, suggesting enhanced ability to capture SM variability at finer spatial scales in these regions. Significant improvements are also evident in wetland- and waterbody-dominated regions from V1.0 to V3.2, although retrievals there still show large variance. The impact of inland water on CYGNSS SM retrieval is discussed in Section IV G.

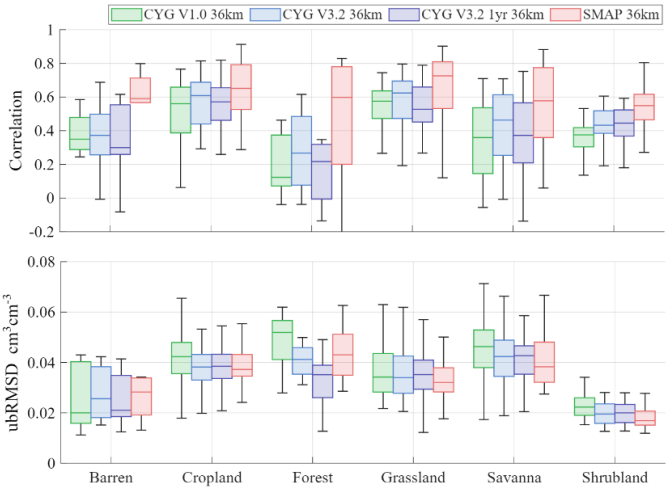


Fig. 8. Retrieval performances (Correlation and ubRMSD) of CYGNSS and SMAP soil moisture products vs ISMN across six major land cover types: Barren, Cropland, Forest, Grassland, Savanna, and Shrubland.

The in-situ SM dataset from ISMN provides an independent validation of CYGNSS SM retrieval quality. Due to the limited number of available stations within each surface type, all sites are grouped into six major land-cover categories: Barren,

This work is licensed under a Creative Commons Attribution 4.0 License. For more information, see https://creativecommons.org/licenses/by/4.0/

This article has been accepted for publication in IEEE Journal of Selected Topics in Applied Earth Observations and Remote Sensing. This is the author's version which has not been fully edited content may change prior to final publication. Citation information: DOI 10.1109/JSTARS.2026.3715093

Cropland, Forest, Grassland, Savanna, and Shrubland. Fig. 8 compares the retrieval performance of the different SM products across these land-cover groups. Per-class ISMN counts and 95% BCa bootstrap confidence intervals on the per-class medians for all three CYGNSS products are reported in Table S2. The CYGNSS V3.2 products (both 36 km and 9 km) show clear improvements over the legacy V1.0 product, particularly in terms of higher correlation and lower ubRMSD relative to in-situ observations. The performance gains are most pronounced over vegetated regions (Croplands, Forests, Savannas, and Shrublands) consistent with the evaluation results obtained using SMAP as the reference dataset. More discussion of SM retrieval performance in vegetated regions is provided in Section IV H.

As shown in Fig. 8, SMAP maintains the highest correlation with in-situ measurements across all land-cover classes. However, it is important to consider the effect of spatial-scale mismatch in such validations. SMAP measures brightness temperature with an effective footprint of approximately 40 km, while CYGNSS reflectivity under coherent scattering conditions has a much finer native resolution on the order of 3 km. In the CYGNSS retrieval algorithm, SM is first estimated at the 3 km subcell level and then aggregated over a 12×12 or 3×3 grid to generate 36 km and 9 km products. When these coarser-scale products are compared with point-scale ISMN measurements, spatial inhomogeneity in SM within the grid cell can introduce significant representativeness error. This mismatch can reduce the observed correlation between satellite and in-situ measurements and may disproportionately affect land cover types with strong local variability, leading to the lower correlation distributions of CYGNSS than SMAP SM against in-situ SM in Fig. 8. The CYGNSS land surface homogeneity dependence is further analyzed in Section IV F.

F. Surface Homogeneity Dependence

The IGBP land cover classification used in this study assigns a dominant land cover type within each 36 km grid cell. The fractional coverage of this dominant class serves as a proxy for land surface homogeneity. Fig. 9 presents scatter plots of ubRMSD from the CYGNSS V3.2 36 km product versus land homogeneity (i.e., the fraction of the dominant land cover) for each IGBP land cover type. A red dashed line in each panel represents the linear regression fit to the data points, with the slope value indicated inside the panel; per-class Pearson correlation r with 95% BCa bootstrap confidence interval, p-value are reported in each panel title. Twelve of fifteen IGBP classes show statistically significant negative correlations between ubRMSD and homogeneity (all $p<0.001$), meaning that retrieval error increases as land surface homogeneity decreases. Two exceptions are noted, Deciduous Broadleaf Forests and Mixed Forests, which show statistically significant positive correlation. As suggested in Fig. 7, these two land covers have the highest ubRMSD medians (in the V3.2 36 km product) among all land covers aside from water bodies. In

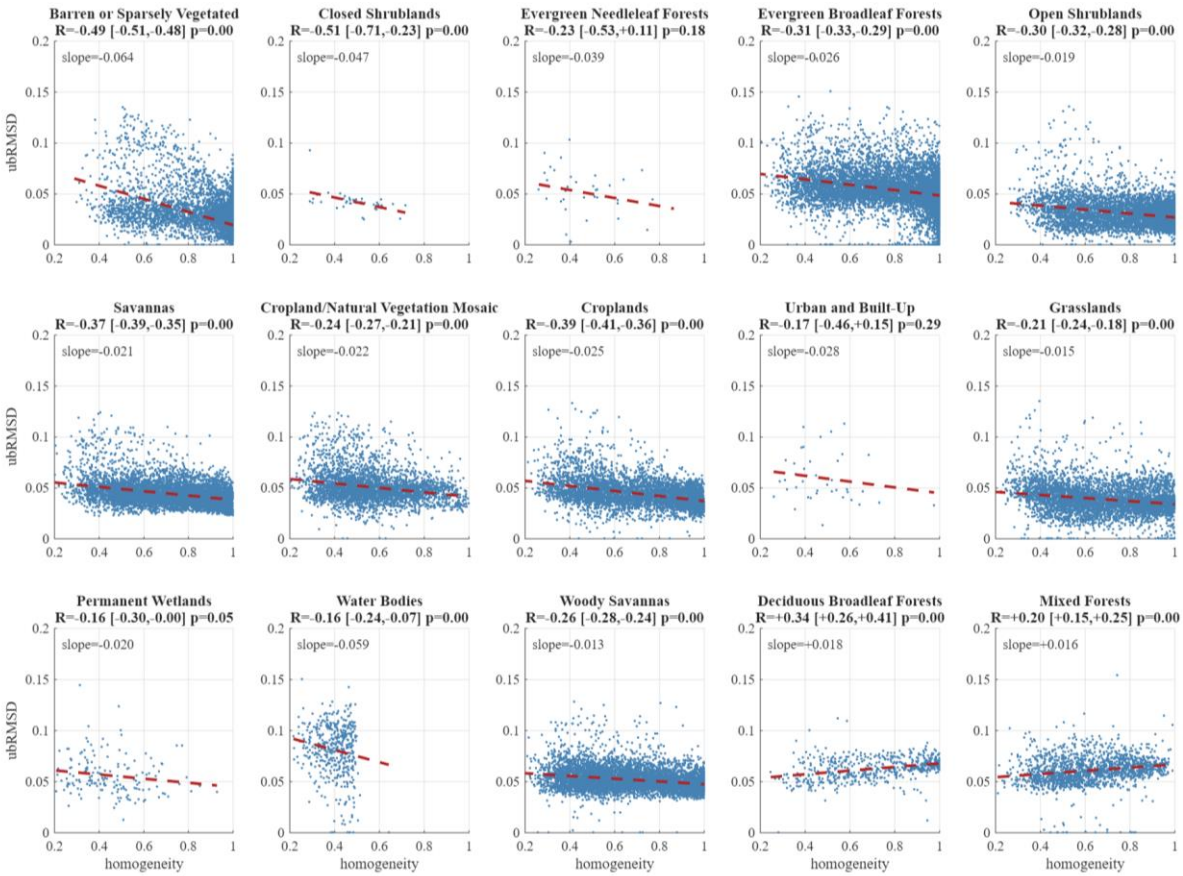


Fig. 9. Scatter plots of SM retrieval ubRMSD vs land homogeneity indicated by the fraction of major land cover of the grid across all IGBP land covers, overlaid by red dashed lines showing the ordinary linear regression line obtained from the scatterers. The regression slopes are reported in each plot. R with 95% confidence interval, two-sided p-values are reported in each panel title.

This work is licensed under a Creative Commons Attribution 4.0 License. For more information, see https://creativecommons.org/licenses/by/4.0/

This article has been accepted for publication in IEEE Journal of Selected Topics in Applied Earth Observations and Remote Sensing. This is the author's version which has not been fully edited content may change prior to final publication. Citation information: DOI 10.1109/JSTARS.2026.3715093

these cases, mixing high-error forested regions with other land cover types that exhibit lower ubRMSD appears to reduce the overall retrieval error in heterogeneous grid cells. Permanent Wetlands show a marginally significant negative correlation. Evergreen Needleleaf Forests and Urban and Built-Up show no statistically significant relationship. The same analysis is not repeated for the 9 km product because the majority of 9 km grids are already highly homogeneous: only 12% of 9 km grids have a dominant land cover fraction below 95%, compared to 60% for 36 km grids.

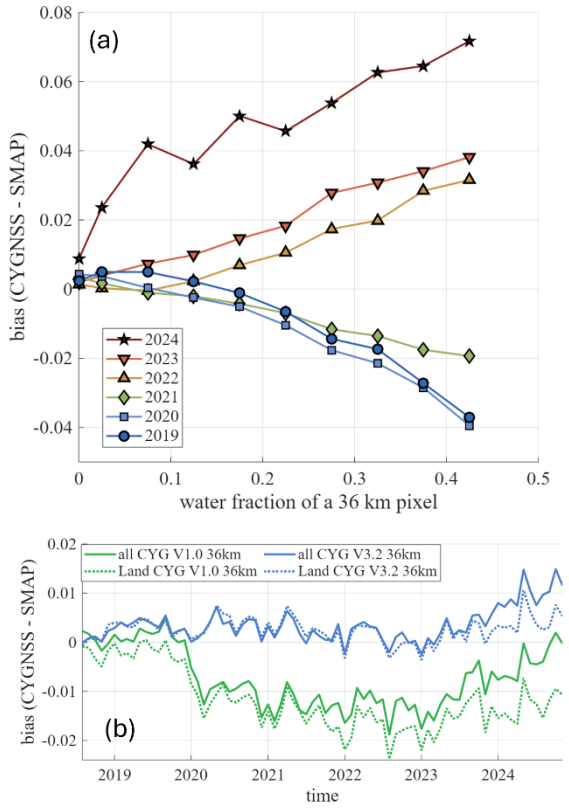


Fig. 10. (a) Annual mean bias between CYGNSS V3.2 and SMAP SM from 2019 to 2024 versus the fractional water coverage within each 36 km land pixel. (b) Time series of mean bias (CYGNSS minus SMAP SM) from 2018 Aug to 2024 Dec. Solid line: all data; Dash line: only land pixel (with zero 36 km grid water fraction).

This trend highlights the challenge of GNSS-R's empirical retrievals over mixed land surfaces. Firstly, the SMAP 36 km SM used as the training reference for an empirical SM retrieval model does not fully represent the local SM variability sensed by GNSS-R at its native kilometer scale resolution, as discussed in Section IV E. The representativeness error caused by the spatial resolution mismatch between CYGNSS and SMAP observables becomes more significant as the land homogeneity decreases. Secondly, the local empirical retrieval model may not adequately describe the blended scattering response within heterogeneous pixels. As discussed in Section II B, the retrieval coefficients are empirically derived for each 3 km grid cell to capture the dominant sensitivity of the effective surface reflectivity (Γ_{eff}) to SM, while statistically accounting for vegetation and roughness effects assumed to be spatially uniform within the 3 km pixel. However, in heterogeneous cells where the surface parameters h, ϵ, τ_v in equation (3) – (4) vary significantly within the CYGNSS footprint, the measured Γ_{eff} becomes spatially nonuniform even for constant SM conditions. Previous study [65] has shown a typical example at a desert-crop land transition zone, in which the CYGNSS measured Γ_{eff}"blurs" across the boundary and requires one CYGNSS footprint size to transition from low to high values. This reflects the spatial variability in scattering properties within the CYGNSS footprint and demonstrates how Γ_{eff} no longer follows the same regression relationship as that established for a homogeneous pixel, resulting in elevated ubRMSD and degraded retrieval performance in these regions. These findings indicate that CYGNSS SM product users should exercise caution when interpreting retrievals near land-cover transitional boundaries, where mixed-surface scattering can degrade performance. Looking ahead, future GNSS-R retrieval frameworks may benefit from improved treatments of surface heterogeneity, such as adaptive gridding based on land-surface similarity or modeling approaches that explicitly account for subpixel variability.

G. Inland Water Influence

The CYGNSS-measured surface effective reflectivity is highly sensitive to inland water due to the strong reflectivity of calm water surfaces. Previous study [29] has shown that spaceborne GNSS-R SM retrievals can become significantly biased when as little as 8–9% of a GNSS-R footprint is occupied by water. Because bistatic reflectivity responds nonlinearly and disproportionately to even small fractions of open water, CYGNSS measurements near water bodies exhibit large positive power biases that propagate directly into the retrieved SM. To mitigate this effect, the CYGNSS SM algorithms (both Versions 1.0 and 3.2) apply the GSWE Pekel water mask, a 30-m, optically derived static product, to exclude reflectivity measurements acquired within approximately 5 km of inland water.

In this study, we evaluate the impact of inland water on the CYGNSS SM product and the effectiveness of this masking approach. The water fraction of each CYGNSS 36 km land pixel is obtained from the MCD12C1 landcover dataset (Section II C). We use the static water-fraction map as a spatial proxy for where dynamic water effects are likely to occur and where CYGNSS specular reflections are likely to fall close to inland water. SMAP SM is used as the reference for fractional-water pixels. SMAP's L-band brightness temperature responds more moderately and predictably to water contamination than CYGNSS reflectivity: fractional water produces a linear and relatively small depression in observed brightness temperature [66], in contrast to the strong nonlinear reflectivity spike seen by CYGNSS. Furthermore, SMAP's descending 6 a.m. overpass occurs under near-thermal-equilibrium conditions between land and inland water, which enables a simple and well-behaved areal-mixing correction for SMAP land brightness temperature [66]. These conditions allow SMAP to provide more reliable SM estimates in mixed land–water pixels.

Fig. 10(a) illustrates how the annual bias between CYGNSS V3.2 and SMAP SM varies with the fractional water coverage within each 36 km land pixel. For each year from 2019 to 2024,

This work is licensed under a Creative Commons Attribution 4.0 License. For more information, see https://creativecommons.org/licenses/by/4.0/

This article has been accepted for publication in IEEE Journal of Selected Topics in Applied Earth Observations and Remote Sensing. This is the author's version which has not been fully edited and content may change prior to final publication. Citation information: DOI 10.1109/JSTARS.2026.3715093

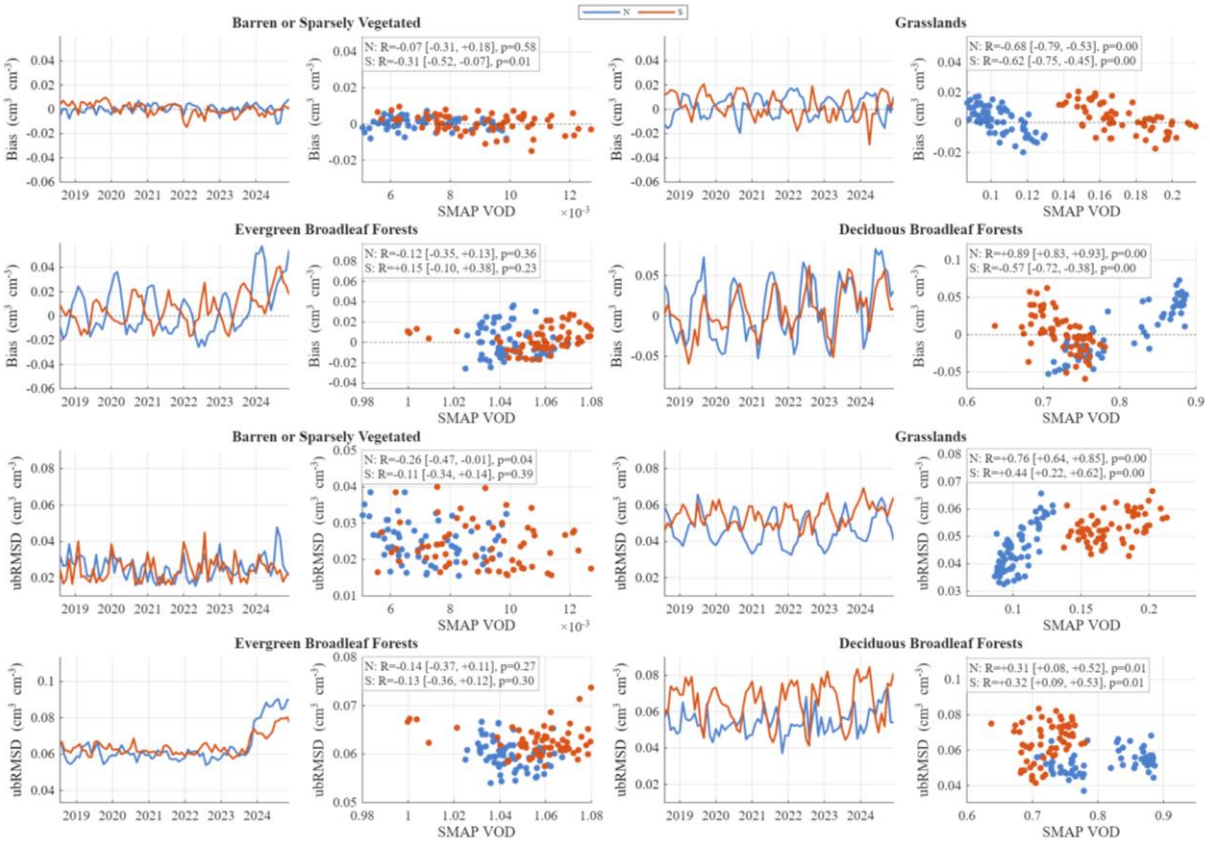


Fig. 11. Monthly bias and ubRMSD between CYGNSS V3.2 36 km and SMAP 36 km SM, shown as time series (left panel in each pair) and as functions of monthly mean SMAP VOD (right panel in each pair), for four land-cover classes: Barren or Sparsely Vegetated, Grasslands, Evergreen Broadleaf Forests, and Deciduous Broadleaf Forests. Northern Hemisphere results are shown in blue and Southern Hemisphere results in orange. Each scatter panel reports Pearson R, the 95% confidence interval, and the p-value.

we compute the annual mean bias, defined as CYGNSS minus SMAP, for all global 36 km pixels. The pixels are grouped into 5% water-fraction bins, and the bias is averaged within each bin; the 0% case is computed separately using all land pixels with no inland water. Two observations follow. First, pixels with zero water fraction show near-zero and temporally stable bias across all years. Second, the slope of the bias-versus-water-fraction curve changes sign over time: it is negative from 2019 through 2021 and becomes positive from 2022 onward, with increasing magnitude through 2024.

To statistically validate the contrast between low- and high-water pixels, we partitioned the global 36 km cells into a high-water-fraction subset, defined as water fraction greater than 0.35, with approximately 1,000 cells, and a low-water-fraction subset, defined as water fraction less than 0.01, with approximately 50,000 cells. We then compare the per-cell CYGNSS minus SMAP bias between the two groups for 2019, 2021, and 2023. Mean absolute bias was significantly larger over high-water cells than over low-water cells in every test year, with differences of 0.037, 0.022, and 0.032 $cm^3\ cm^{-3}$ in 2019, 2021, and 2023, respectively, all with $p < 0.001$. The bias growth rate was also significantly steeper in the high-water subset, $1.88 \times 10^{-2}\ cm^3\ cm^{-3}\ yr^{-1}$, with a 95% confidence interval of $[1.78, 1.98] \times 10^{-2}$, than in the low-water subset, $-2.0 \times 10^{-4}\ cm^3\ cm^{-3}\ yr^{-1}$. This gives a difference in mean drift rates of $1.90 \times 10^{-2}\ cm^3\ cm^{-3}\ yr^{-1}$ between the high- and low-water subsets, with a 95% confidence interval of $[1.80, 2.00] \times 10^{-2}$. These results show that the multi-year positive bias drift is significantly larger in pixels with substantial water content and is essentially low in pixels classified as land.

A plausible mechanism is that pixels which transitioned from land to water after 2021, the last update of Pekel water mask, were still treated as land during the retrieval model training. These pixels likely exhibited high reflectivity variance and introduced water-contaminated samples into the land-retrieval training set, forcing the regression solution toward a mean-square-error compromise. Under this compromise, purely land pixels may be biased low, producing negative bias, while water-contaminated pixels may be biased high, producing positive bias. As the training period advances into later years, this imbalance may shift the locally fitted regression coefficients toward a systematically positive bias. The steadily increasing positive bias after 2021 is consistent with an increasing contribution from pixels affected by dynamic land–water changes that are not captured by the static mask. This explanation is consistent with both the sign reversal of the bias-versus-water-fraction slope after 2021 and the fact that the static Pekel mask cannot capture land-to-water transitions occurring after its last update. Flooding, inundation, and long-term hydrological change linked to climate and human activity could be candidate drivers of such transitions.

This work is licensed under a Creative Commons Attribution 4.0 License. For more information, see https://creativecommons.org/licenses/by/4.0/

This article has been accepted for publication in IEEE Journal of Selected Topics in Applied Earth Observations and Remote Sensing. This is the author's version which has not been fully edited; content may change prior to final publication. Citation information: DOI 10.1109/JSTARS.2026.3715093

To examine how the inland-water-contaminated pixels relate to the multi-year bias drift identified in Section IV D, Fig. 10(b) shows the monthly mean bias (CYGNSS minus SMAP) time series from August 2018 through December 2024 for the V3.2 and V1.0 products, computed first over all pixels and then over land-only pixels with water fraction equal to 0. When only land pixels are retained, the post-2023 upward bias trend that is prominent in the all-pixel time series of Fig. 5 is substantially reduced for both the V3.2 and V1.0 products. This suggests that the multi-year drift is consistent with inland-water-contaminated pixels rather than with the bulk land retrieval.

These results suggest an important limitation of the static-water-mask approach used in CYGNSS and the broader GNSS-R SM community, which typically relies on the Pekel water mask or similar static optical products. The Pekel mask has not been updated since 2021, so any land-to-water transitions occurring after that date are not captured. Besides, optical mask products tend to underestimate water surfaces that are partially or fully obscured by vegetation, whereas CYGNSS has demonstrated sensitivity to such hidden water bodies through its microwave-based specular reflectivity [67]. Mitigating these limitations is a natural direction for future work. The recently released CYGNSS-based dynamic inland waterbody map [68] leverages multi-year global reflectivity observations and is well suited to distinguish land measurements from water-contaminated returns at the relevant timescale. Integrating such a dynamic, CYGNSS-derived water mask into the SM retrieval framework would allow direct testing of the attribution proposed in this section and has the potential to improve the robustness of future CYGNSS SM products. For future work, region-specific case studies in areas with documented multi-year hydrological change would provide a complementary line of evidence.

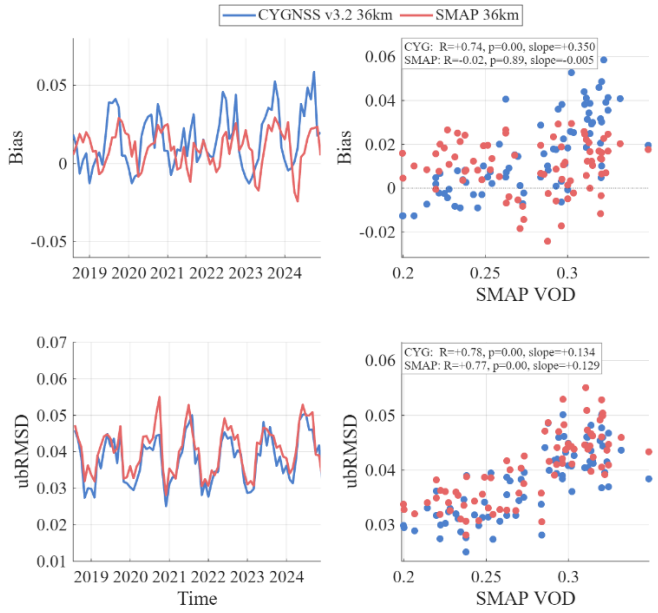


Fig. 12. Monthly bias and ubRMSD of CYGNSS V3.2 36 km (blue) and SMAP 36 km (red) SM against ISMN in-situ observations over Shrubland, Grassland, and Cropland sites in the Northern Hemisphere. Time series (left) and scatter against monthly mean SMAP VOD (right) are shown for both bias (top) and ubRMSD (bottom).

H. Vegetation Influence

To examine the role of vegetation in CYGNSS SM retrieval performance, we narrow the analysis to four land-cover classes that span a wide range of both VOD magnitude and seasonal VOD variability: Barren or Sparsely Vegetated areas (low VOD, weak seasonality), Grasslands (moderate VOD, strong seasonality), Evergreen Broadleaf Forests (high VOD, weak seasonality), and Deciduous Broadleaf Forests (high VOD, strong seasonality). Pixels with water fraction higher than 0.05 and homogeneity less than 0.6 are discarded. For each class, Fig. 11 shows the monthly time series of CYGNSS-versus-SMAP bias and ubRMSD over the seven-year record, along with the corresponding scatterplots against monthly mean SMAP VOD, separated by hemisphere. Pearson correlation coefficients and their statistical significance (95% confidence interval and p-value) are reported in each scatter plot's panel.

In the two classes with strong seasonal VOD variation, Grasslands and Deciduous Broadleaf Forests, ubRMSD between CYGNSS and SMAP increases significantly with VOD in both hemispheres. For Grasslands, the correlations are $R = +0.76$ in the Northern Hemisphere and $R = +0.44$ in the Southern Hemisphere, both with $p < 0.01$. For Deciduous Broadleaf Forests, the correlations are $R = +0.31$ in the Northern Hemisphere, with $p = 0.01$, and $R = +0.32$ in the Southern Hemisphere, with $p = 0.01$. In contrast, for the two classes with weak seasonal VOD variation, Barren or Sparsely Vegetated areas and Evergreen Broadleaf Forests, the ubRMSD–VOD correlations are weak and mostly non-significant. For Barren or Sparsely Vegetated areas, the correlations are $R = -0.26$ in the Northern Hemisphere, with $p = 0.038$, and $R = -0.11$ in the Southern Hemisphere, with $p = 0.386$. For Evergreen Broadleaf Forests, the correlations are $R = -0.14$ in the Northern Hemisphere, with $p = 0.269$, and $R = -0.13$ in the Southern Hemisphere, with $p = 0.298$. All correlations are computed using $n = 77$ monthly aggregated points, and the full 95% confidence intervals are reported in the corresponding panels of Fig. 11. The positive ubRMSD–VOD correlations in the seasonally vegetated classes indicate that CYGNSS and SMAP increasingly disagree with each other as VOD rises

The bias–VOD relationship is more complex and varies sharply among land-cover classes, with $n = 77$ monthly aggregated points for each land-cover class and hemisphere. Grasslands show a strong negative bias–VOD correlation in both hemispheres, with $R = -0.68$ in the Northern Hemisphere and $R = -0.62$ in the Southern Hemisphere, both with $p < 0.001$. This indicates that CYGNSS tends to be systematically lower than SMAP under high vegetation density and higher than SMAP under low vegetation density.

Deciduous Broadleaf Forests display nearly in-phase behavior in both hemispheres, which deviates from the expected seasonal pattern. Bias is very strongly positively correlated with VOD in the Northern Hemisphere, with $R = +0.89$ and $p < 0.001$, but moderately negatively correlated with VOD in the Southern Hemisphere, with $R = -0.57$ and $p < 0.001$. The opposite signs suggest that VOD alone does not provide a consistent explanation for the CYGNSS-versus-SMAP bias in this land-cover class. Instead, the bias–VOD relationship likely reflects the combined influence of vegetation

This work is licensed under a Creative Commons Attribution 4.0 License. For more information, see https://creativecommons.org/licenses/by/4.0/

This article has been accepted for publication in IEEE Journal of Selected Topics in Applied Earth Observations and Remote Sensing. This is the author's version which has not been fully edited content may change prior to final publication. Citation information: DOI 10.1109/JSTARS.2026.3715093

density and hemisphere-dependent seasonal or climatic covariates. In fact, the North and South hemisphere Deciduous Broadleaf Forest regions are dominated by different climate regimes: temperature-driven temperate phenology in eastern North America and water-driven, monsoon-coupled phenology in tropical-to-subtropical South America [69]. As a result, the same VOD value can correspond to different combinations of soil moisture, temperature, and surface conditions in the two regions.

Evergreen Broadleaf Forests, with weak VOD seasonality in both hemispheres, show no significant bias–VOD relationship (Northern $R = -0.12$, $p = 0.358$; Southern $R = +0.15$, $p = 0.226$). Barren or sparsely vegetated surfaces show a hemispheric contrast: the Northern Hemisphere has no significant correlation ($R = -0.07$, $p = 0.580$), whereas the Southern Hemisphere shows a moderate, statistically significant negative correlation ($R = -0.31$, $p = 0.011$), in the same direction as the Grassland response. Given the very narrow VOD range in barren regions (~0.005–0.015), this correlation should be interpreted as a weak modulation rather than as a physically large slope effect. Full 95 % confidence intervals for all bias–VOD correlations are reported in Fig. 11.

To assess how CYGNSS and SMAP compare against an independent reference under varying vegetation density, we evaluate both products against ISMN in-situ observations from Shrubland, Grassland, and Cropland stations in the Northern Hemisphere. The results are shown in Fig. 12 and include 221 sites and 77 months. The monthly bias of CYGNSS against ISMN is strongly correlated with VOD, with $R = +0.74$, $p < 0.001$, and a slope of +0.350 $cm^3\ cm^{-3}$ per VOD unit. In contrast, the monthly bias of SMAP against ISMN shows no significant VOD dependence, with $R = -0.02$, $p = 0.89$.

The monthly ubRMSD of both products against ISMN increases with VOD with closely matching slopes. For CYGNSS, $R = +0.78$ and the slope is +0.134; for SMAP, $R = +0.77$ and the slope is +0.129. Both correlations are significant at $p < 0.001$. A formal slope-difference test on the monthly aggregates confirms that the two ubRMSD–VOD slopes are not statistically distinguishable. The slope difference is +0.005, with a 95% confidence interval of [−0.009, +0.019] and a two-sided p-value of 0.48, using 77 months of data. Thus, within this ISMN-based monthly comparison, there is no statistical evidence that CYGNSS ubRMSD increases more rapidly with VOD than SMAP ubRMSD. This suggests that CYGNSS does not exhibit detectably stronger vegetation-related error growth than SMAP at these ISMN sites, despite the absence of an explicit vegetation correction in the empirical CYGNSS retrieval model.

Previous modeling studies for passive microwave radiometry [70] have shown that the vegetation optical depth (VOD) τ_v in (4) is linearly related to Vegetation Water Content (VWC) through $\tau_v = b \cdot VWC$, where the coefficient b at L-band depends on land-cover type. Because VWC exhibits strong seasonal variation, this model implies that the seasonal cycle of VOD arises directly from the seasonal cycle of VWC. Although the applicability of this linear VOD–VWC relationship to GNSS-R systems remains an active area of investigation, earlier study [25] has shown the dependence of CYGNSS data on VWC and the potential utility of applying the VOD-VWC linear model to reflectometry systems like CYGNSS. Both CYGNSS V1.0 and V3.2 empirical SM retrievals are trained within fixed multi-year periods under an implicit static-vegetation assumption, and therefore represent vegetation effects implicitly through the statistical relationships contained in the training data. This limitation may contribute to vegetation-dependent biases when seasonal or interannual vegetation conditions depart from those learned relationships.

In this study, the bias-VOD relationship is strong for CYGNSS vs ISMN but absent for SMAP vs ISMN, indicating that the systematic component of CYGNSS error is more vegetation-sensitive than SMAP's. By contrast, the similar CYGNSS–ISMN and SMAP–ISMN ubRMSD–VOD slopes indicate that CYGNSS does not exhibit substantially stronger vegetation-dependent random-error growth than SMAP when evaluated against in-situ observations. However, the concurrent increase in CYGNSS–SMAP ubRMSD with VOD shows that the two satellite products become less mutually consistent in denser vegetation. This suggests that the vegetation-dependent disagreement between CYGNSS and SMAP is not simply due to a stronger degradation of one product relative to in-situ observations. Instead, it may reflect differences in how the two satellite systems respond to vegetation. Besides, this result indicates that SMAP VOD should be interpreted cautiously as an empirical vegetation proxy in CYGNSS SM retrieval rather than a sensor-neutral representation of vegetation effects. Additional tests using vegetation descriptors that are independent of SMAP, such as optical sensor derived NDVI or land-cover-specific vegetation parameters, would be needed to determine whether SMAP VOD is optimal for representing vegetation effects in CYGNSS SM retrievals.

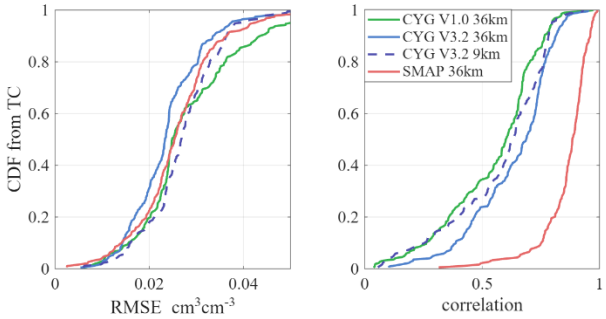


Fig. 13. CDFs of RMSE (left) and correlation (right) derived from Triple Collocation analysis for CYGNSS and SMAP soil moisture retrievals.

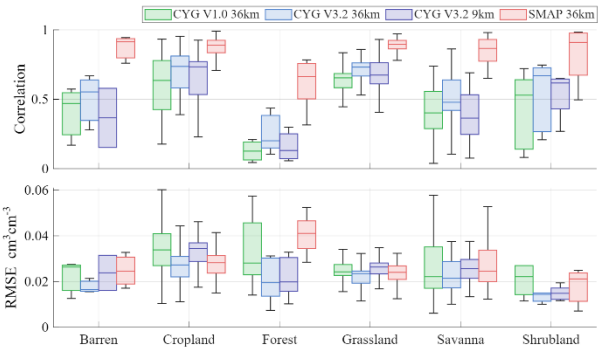


Fig. 14. TC-based correlation and RMSE of CYGNSS and SMAP soil moisture retrievals across different land cover types.

This work is licensed under a Creative Commons Attribution 4.0 License. For more information, see https://creativecommons.org/licenses/by/4.0/

This article has been accepted for publication in IEEE Journal of Selected Topics in Applied Earth Observations and Remote Sensing. This is the author's version which has not been fully edited content may change prior to final publication. Citation information: DOI 10.1109/JSTARS.2026.3715093

I. Triple Collocation assessment

The Triple Collocation (TC) algorithm described in Section III B is applied in order to estimate the correlation and RMSE of the CYGNSS and SMAP SM products relative to the true soil moisture state. As demonstrated in Sections IV H, both retrievals exhibit strong seasonal climatological signals driven by vegetation dynamics and other environmental factors. These seasonal signals can introduce spurious correlations among the datasets, thereby violating the TC assumption that retrieval errors are mutually uncorrelated. To reduce this risk and improve the validity of the TC estimates, the monthly mean is removed from each SM time series prior to applying the TC algorithm.

Fig. 13 presents cumulative distribution functions (CDFs) of RMSE and correlation values derived from the TC analysis. The CYGNSS V3.2 products (both 36 km and 9 km) exhibit clear improvements over the legacy V1.0 product. In the RMSE panel (left), the V3.2 CDFs are consistently shifted leftward, indicating lower error magnitudes across the distribution. In the correlation panel (right), the SMAP 36 km product outperforms all CYGNSS versions, demonstrating the strongest agreement with the latent truth. Nevertheless, the CYGNSS V3.2 products show substantial improvements over V1.0, with their correlation CDFs shifted rightward and exhibiting reduced spread, reflecting improved consistency and accuracy in retrievals.

Fig. 14 illustrates the distribution of correlation and RMSE values derived from TC analysis across six major land cover classes. SMAP consistently shows higher correlation with the latent SM truth across all land cover types. However, the CYGNSS V3.2 36 km product demonstrates lower RMSE than SMAP in several land cover classes, including Barren, Forest, Savanna, and Shrubland. Among the CYGNSS products, V3.2 (both 36 km and 9 km) shows clear improvements over V1.0, with higher correlations and reduced RMSE across most land covers. Interestingly, the V3.2 36 km product outperforms the 9 km product in many cases, suggesting a resolution mismatch issue inherent in the design of the retrieval model. These TC-based findings are consistent with the bias and ubRMSD patterns in Section IV E, where the ISMN in-situ SM is used as the reference.

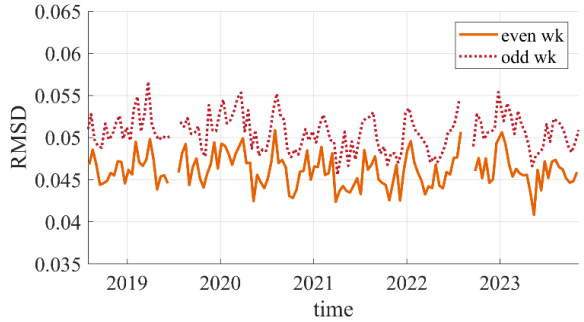


Fig. 15. Weekly RMSD between SMAP SM and CYGNSS even-week and odd-week SM. The CYGNSS SM retrieval model is trained on the even-week dataset and evaluated on both even-week and odd-week datasets.

V. Retrieval Model Stability Diagnostic

Most current GNSS-R SM retrieval algorithms rely on historical data within a fixed time window to train empirical models. As shown in Section IV D, both the CYGNSS V1.0 and V3.2 products exhibit a degradation in performance manifested as sharp increases in RMSD and ubRMSD immediately following the end of their respective training periods (see Fig. 5). This degradation indicates that retrieval-model parameters fitted on the training window do not always remain optimal when applied to data outside that window, indicating a model stability issue. This section diagnoses where in the global retrieval domain this loss of stability is most pronounced and identifying the data-regime conditions under which it arises.

To evaluate potential model stability issues in the CYGNSS V3.2 retrieval model, we apply a temporal split-sample cross-validation strategy that divides the multiyear dataset into two disjoint subsets according to even and odd calendar weeks. This temporal partition preserves the seasonal and interannual variability of SM while separating temporally adjacent observations into different subsets. The retrieval model is trained using the even-week data and then evaluated on both the even-week (training) and odd-week (testing) datasets. Fig. 15 shows the weekly RMSD between CYGNSS and SMAP under this train–test configuration.

For each grid cell we define the stability index

$$SI = \frac{RMSD_{test} - RMSD_{train}}{RMSD_{train}} * 100 \qquad (15)$$

Where $RMSD_{train}$ is the RMSD computed on the even-week subset for training and $RMSD_{test}$ is the RMSD on the odd-week subset for testing. SI $\approx$ 0 indicates that the trained model performs as well on out-of-sample data as on in-sample data; SI $>$ 0 indicates that the fitted on the training subset extrapolates less accurately to the testing subset. SI is the primary diagnostic metric used in this section and is computed at the 36 km grid level for the global analysis (Section V A) and at the 3 km subcell level for the local case study (Section V B).

A. Global Model Stability Diagnostic

Firstly, we examine the problem from a macro perspective. Fig. 16(a) maps the RMSD percentage increase from training to testing against two descriptors of each 36 km grid cell: (i) the mean CYGNSS Γ_{eff} and SMAP SM correlation, and (ii) the mean number of CYGNSS–SMAP matchups across the 12×12 underlying 3 km subcells. All global 36 km cells are binned in this 2-D space, and the color in each bin shows the median RMSD increase for the cells it contains. The figure reveals a clear pattern: cells with either fewer matchups or weaker Γ_{eff}–SM correlation tend to experience larger increases in RMSD when transitioning from training to testing, indicating reduced model stability in these regimes.

To illustrate these relationships more concretely, four regions (a–d) spanning distinct combinations of correlation and matchup density are highlighted in Fig. 16(a). The corresponding distributions of RMSD (train vs. test) and RMSD percentage increase are shown in Fig. 16(b)–(c), and their statistics (SI median and 95% confidence interval) are reported in Table 2. Two-sided Wilcoxon signed-rank tests confirm that the train-to-test RMSD increase is statistically distinct from

This work is licensed under a Creative Commons Attribution 4.0 License. For more information, see https://creativecommons.org/licenses/by/4.0/

This article has been accepted for publication in IEEE Journal of Selected Topics in Applied Earth Observations and Remote Sensing. This is the author's version which has not been fully edited content may change prior to final publication. Citation information: DOI 10.1109/JSTARS.2026.3715093

zero in every region (all $p<0.001$). A summary of each region's behavior is provided below:

1) Region a (high correlation, high matchup count): Retrievals here exhibit the highest train-test stability. Abundant matchup data and a strong linear reflectivity–SM relationship support a well-constrained regression model. The train–test RMSD difference is minimal (SI close to 0).
2) Region b (high correlation, low matchup count): Strong SM variability is well captured by both sensors, but training data is sparse. The limited sample size yields a wider RMSD spread and a moderate RMSD increase, consistent with the overfitting regime familiar from machine-learning practice.
3) Region c (low correlation, high matchup count): Typically found in arid regions with low SM variability. Although RMSD is small due to the nearly flat SM dynamics, the weak Γ_{eff}–SM relationship could produce large SI and high variance.
4) Region d (low correlation, low matchup count): Retrieval quality is poor in both training and testing, as weak Γ_{eff}–SM sensitivity and sparse data jointly limit model performance. Train–test RMSD differences remain small not because the model generalizes well, but because both subsets perform similarly poorly, a pattern consistent with the underfitting regime.

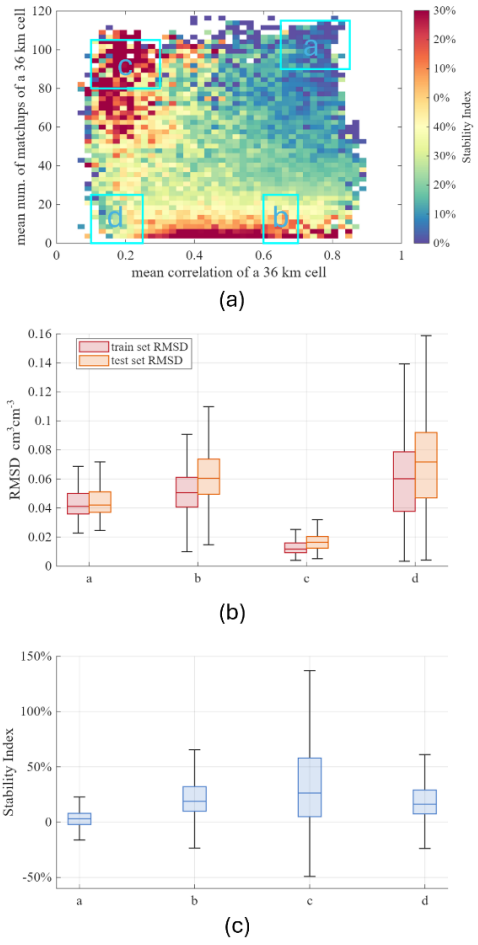


Fig. 16. (a) 2D map of RMSD percentage increase against the mean correlation between CYGNSS Γ_{eff} and SMAP SM, and the mean of the number of CYGNSS-SMAP measurement matchups of each 3 km subcell, followed by (b) the distributions of train and test sets RMSD and (c) RMSD percentage increase of the four highlighted zones (boxes a-d).

Across the four regions highlighted in Fig. 16, the CYGNSS retrieval model exhibits several distinct stability regimes. Region a represents the desired operating regime: strong Γ_{eff}–SM correlation and abundant matchup data enable a well-constrained regression model whose training and testing RMSD are nearly identical. Region b is consistent with the overfitting regime: although the high correlation indicates that the linear model is physically valid and that Γ_{eff} is strongly sensitive to SM, the limited number of matchups constrains the robustness of the fitted parameters, leading to noticeably worse performance on the testing set. Region c, which contains most arid and desert pixels, displays a different kind of stability limitation. Here the linear Γ_{eff}–SM relationship remains valid, but the SM distribution occupies a very narrow low-moisture range, giving the regression model little dynamic range to learn from. Training RMSD is small simply because SM varies minimally, yet the estimated slope and intercept become sensitive to small fluctuations or calibration differences, producing disproportionately large relative SI on the test set. This behavior is driven by the data distribution, rather than overfitting or underfitting. Finally, Region d corresponds to the most challenging retrieval environments, where both Γ_{eff}–SM correlation and matchup counts are low; in these locations, limited signal sensitivity and sparse training data jointly degrade model performance, resulting in consistently poor retrieval accuracy in both training and testing subsets.

It is important to note that the CYGNSS V3.2 model benefits from being trained with nearly five years of CYGNSS–SMAP matchups, yielding substantially more samples per 3 km subcell than earlier GNSS-R SM products (including CYGNSS V1.0), which were trained using only one year of data. This increased data volume mitigates many of the model stability problems characteristic of low-sample regimes. The contrast between V3.2 and V1.0 reflects the same mechanisms seen in Fig. 16: retrievals trained in low-matchup, weak-correlation environments (analogous to regions b and d) are the most vulnerable to low train-test stability. Many existing empirical CYGNSS and other GNSS-R SM products also rely on one-year training windows and sub-cell regression frameworks. These products will therefore encounter the same stability problems discussed here, highlighting the need for longer training periods or more robust model formulations going forward.

Table 2 Four region SI Statistics

Region	n	Median SI (%)	95% CI	p-value
a	558	3.04	[2.00, 3.70]	< 0.001
b	2187	18.86	[17.90, 19.60]	< 0.001
c	455	26.28	[21.42, 29.96]	< 0.001
d	2232	16.21	[15.38, 16.94]	< 0.001

B. Local Model Stability Diagnostic

We next investigate the problem from a micro-scale perspective by examining a specific 36 km grid cell centered at 34.99°N, 119.32°W in Southern California, as shown in Fig. 17(a). This grid cell corresponds to Region b in Fig. 16. This

This work is licensed under a Creative Commons Attribution 4.0 License. For more information, see https://creativecommons.org/licenses/by/4.0/

This article has been accepted for publication in IEEE Journal of Selected Topics in Applied Earth Observations and Remote Sensing. This is the author's version which has not been fully edited content may change prior to final publication. Citation information: DOI 10.1109/JSTARS.2026.3715093

cell contains 144 subcells, which exhibit a nearly uniform distribution of Γ_{eff}–SM correlations (mean ≈ 0.5) and an exponential distribution of CYGNSS–SMAP matchup counts (mean ≈ 20), as shown in Fig. 17(b) and 17(c), respectively. This combination provides a natural testbed to examine how correlation strength and data availability jointly influence model stability inside one 36 km cell.

To analyze the retrieval behavior in more detail, we categorize the subcells into four regions based on correlation and matchup availability, similar to Section V A:

1) R1: High correlation (> 0.5) and high matchup count (> 20) — 27 subcells
2) R2: High correlation, low matchup count (<20) — 28 subcells
3) R3: Low correlation (≤ 0.5), high matchup count— 29 subcells
4) R4: Low correlation, low matchup count — 25 subcells

In addition to the cell-level SI metric defined at the start of this section, we use model parameters stability as a complementary diagnostic at the local scale. Parameter stability refers to the consistency of the empirical regression coefficients (in this case, slope and intercept) between the training and testing sets. A model with high parameter stability maintains similar parameter values across the two subsets, meaning the parameterization optimized on the training data remains effective when applied to independent samples. Conversely, large deviations in the regression slope or intercept between training and testing indicate low parameter stability.

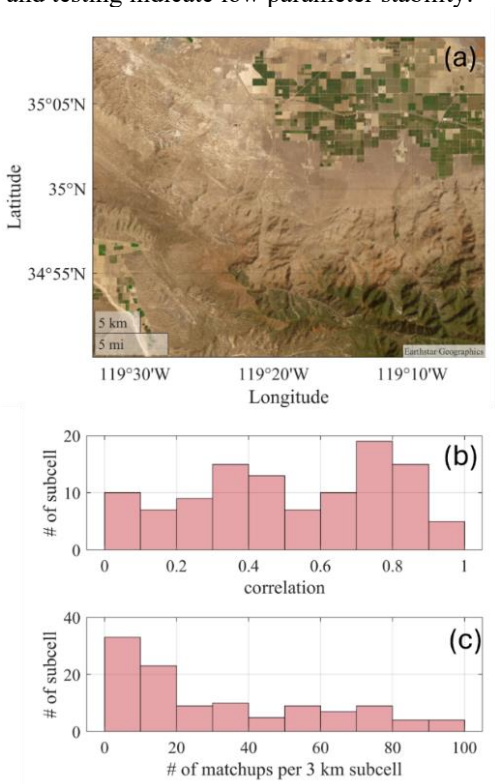


Fig. 17. (a) selected 36 km cell centered at 34.99°N and 119.32°W; (b) histogram of the correlation between CYGNSS reflectivity and SMAP SM of all local 3 km subcells; (c) histogram of number of CYGNSS and SMAP data matchups of all local 3 km subcells

Fig. 18(a) and 18(b) show the percentage changes in slope and intercept for each region R1–R4. Parameter stability statistics are reported in Table 3. Median |Δβ| grows from 19% in R1, the stable baseline, to 64% in R2, 61% in R3, and 124% in R4; median |Δintercept| follows the same ordering (9.1%, 43%, 14%, and 94.7%, respectively). 95% confidence interval is also reported in the table. As shown in Table 3 column 5, One-sided Mann-Whitney U tests confirm that |Δβ| in R2, R3, and R4 is statistically larger than R1 and that |Δintercept| in R2 and R4 is statistically larger than R1 (all $p<0.001$). The intercept shift in R3 is not statistically distinguishable from R1 ($p=0.106$), suggesting that in the R3 regime, the regression slope is primarily unstable, while the intercept is comparatively stable.

In Region R1, both parameters exhibit minimal variation between training and testing, consistent with the stable behavior expected from locations with strong Γ_{eff}–SM correlation and abundant matchup data. Regions R2 and R3, each limited by either insufficient data (R2) or weak Γ_{eff}–SM sensitivity (R3), show broader parameter distributions and increased median deviations. Region R4 exhibits the lowest parameter stability: both slope and intercept exhibit the largest spreads and highest median percentage changes, indicating that models trained under simultaneously data-sparse and weak-correlation yield empirical regressions whose coefficients depend strongly on the specific samples present in the training subset.

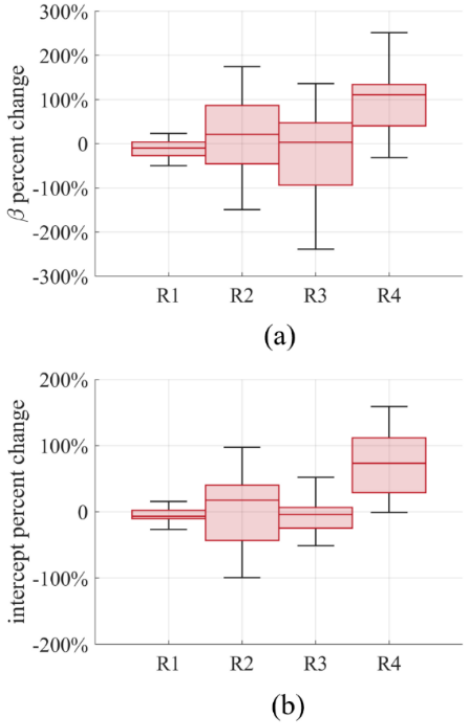


Fig. 18. (a) Model slope (β) percentage change and (b) model intercept percentage change from training to testing set from regions R1 to R4.

The reduced parameter stability observed in Regions R2–R4 directly contributes to the elevated SI and large train–test RMSD gaps identified in the cross-validation analysis of this 36 km cell. Importantly, the same mechanisms identified in this local case also operate globally and therefore extend naturally to the broader train–test discrepancies documented in Section

This work is licensed under a Creative Commons Attribution 4.0 License. For more information, see https://creativecommons.org/licenses/by/4.0/

This article has been accepted for publication in IEEE Journal of Selected Topics in Applied Earth Observations and Remote Sensing. This is the author's version which has not been fully edited and content may change prior to final publication. Citation information: DOI 10.1109/JSTARS.2026.3715093

IV D. These findings highlight the need for retrieval model improvements and additional quality-control mechanisms. Future versions of the CYGNSS SM product will include new quality flags designed to identify subcells exhibiting low parameter stability due to limited matchup data or weak Γ_{eff}–SM correlation. More broadly, because most existing GNSS-R spaceborne SM retrievals adopt similar empirical frameworks that rely on SMAP as the reference and use subcell-based regression, stability should be considered a fundamental design criterion for improving the robustness and reliability of GNSS-R SM products.

Table 3 Model parameter stability statistics

Region	n	Median $\lvert\Delta\beta\rvert$ (%)	95% CI	p-value (M-W vs R1)
R1	27	19.41	[10.20, 27.37]	-
R2	20	63.94	[35.29, 124.66]	< 0.001
R3	29	60.71	[38.81, 101.71]	< 0.001
R4	14	124.09	[96.28, 164.97]	< 0.001
Region	n	Median |Δintercept| (%)	95% CI	P (M-W vs R1)
R1	27	9.1	[6.7, 13.2]	-
R2	20	43	[27.2, 63.6]	< 0.001
R3	29	14	[4.6, 26.8]	0.106
R4	14	94.7	[54.7, 118.1]	< 0.001

VI. Discussion

The results presented in this study demonstrate a measurable link between Level-1/Level-0 calibration quality and the CYGNSS SM retrieval performance. The CYGNSS V3.2 engineering calibration improvements, including dynamic EIRP estimation, refined noise-floor correction, and the compensation for thermal variations in receiver electronics, yield measurable improvements in SM retrieval accuracy, temporal stability, and bias behavior. The reduction in long-term drift and the correction of GPS Flex Power induced bias artifacts indicate that surface reflectivity Γ_{eff} is now being calibrated with improved accuracy. These findings therefore highlight the importance of continual calibration refinement and indicate that CYGNSS is maturing into a stable, long-duration land remote-sensing instrument capable of approaching the temporal stability needed for longer-term SM applications.

The spatial performance patterns observed in Section IV reflect several fundamental environmental constraints on empirical GNSS-R SM retrieval. The three principal factors (surface homogeneity, inland water, and vegetation) that modulate CYGNSS V3.2 SM performance against SMAP are summarized in Table 4 with their observed effects, hypothesized mechanisms, and suggested directions for future investigations. Land-surface heterogeneity introduces representativeness limitations: SMAP, which serves as the training reference for CYGNSS, has a much coarser effective footprint than the native kilometer-scale GNSS-R sensitivity. As a result, SMAP cannot fully describe the local SM variability sensed by CYGNSS, and the sub-cell spatial information available in CYGNSS is not fully exploited under the current retrieval framework. Evidence suggests that inland water bodies might impose additional challenges in CYGNSS SM retrieval: Small bodies of water disproportionately increase bistatic reflectivity, producing systematic positive SM biases that the static Pekel water mask does not fully capture. The mask's limited temporal updates and reliance on optical imagery, which can underestimate water beneath vegetation, further constrain its effectiveness. It should be noted that the inland-water analysis presented here provides a plausible and supported explanation for the observed bias behavior, but a direct demonstration of the inland-water impact on the SM product will require future work using dynamic GNSS-R water masking and region-specific case studies. Vegetation phenology introduces yet another time-varying driver of retrieval performance: seasonal dynamics in biomass and vegetation water content modulate reflectivity attenuation, while the empirical model only implicitly accounts for vegetation effects through statistical relationships in the training data. Together, these factors help explain the spatial structure of CYGNSS V3.2 SM retrieval inconsistency against SMAP, highlight the limitations of current ancillary datasets, and motivate advances in adaptive spatial gridding, dynamic water masking, and vegetation-aware modeling for GNSS-R SM retrieval.

Current GNSS-R systems cannot fully separate SM information from the contributions of terrain roughness and vegetation scattering in the measured signal. As a result, SM retrievals rely heavily on empirical models trained against reference datasets such as SMAP. The dense spatial coverage, frequent revisit, and multi-incidence-angle sampling provided

Table 4 Summary of factors degrading CYGNSS V3.2 SM performance against SMAP, with hypothesized mechanism and directions for future work

Factor	Effect on V3.2 vs SMAP	Hypothesized mechanism	Future Investigation
Surface Homogeneity (Section IV F)	ubRMSD increases as in-cell homogeneity decreases (12 of 15 IGBP land classes)	Spatial resolution mismatch between the CYGNSS footprint and SMAP 36 km grid cell	Adaptive spatial gridding and explicit sub-pixel variability modeling
Inland Water (Section IV G)	Higher and annually increasing retrieval bias in cells with high inland-water fraction	Bistatic reflectivity nonlinearly amplified by inland-water bodies; limited temporal dynamics of Pekel's static water mask	Regional case studies combined with hydrological records; testing of a dynamic water mask
Vegetation (Section IV H)	Retrieval bias and ubRMSD are correlated with SMAP VOD in vegetated regions	Vegetation phenology-driven attenuation of surface effective reflectivity, exacerbated by the static vegetation assumption in the retrieval model	Vegetation-aware retrieval modeling and incorporation of additional vegetation descriptors (e.g., NDVI from optical sensors)

This work is licensed under a Creative Commons Attribution 4.0 License. For more information, see https://creativecommons.org/licenses/by/4.0/

This article has been accepted for publication in IEEE Journal of Selected Topics in Applied Earth Observations and Remote Sensing. This is the author's version which has not been fully edited content may change prior to final publication. Citation information: DOI 10.1109/JSTARS.2026.3715093

by CYGNSS make empirical retrievals feasible and effective. However, the results in this study reveal that such empirical models can exhibit model stability limitations, with retrieval performance degrading in specific environmental and data-limited conditions. As demonstrated in Section V, these limitations arise primarily from three factors: insufficient training samples (data sparsity), weak Γ_{eff}–SM sensitivity (particularly in vegetated or complex terrain), and limited SM dynamic range (common in arid regions). In these regimes, the regression models learned during the training window do not extrapolate well to new conditions, leading to time-split train–test performance degradation. Although the multi-year training dataset used in CYGNSS V3.2 helps mitigate many of these issues, it does not fully eliminate them, indicating that model stability in those specific areas is still a constraint in most current empirical GNSS-R SM retrieval frameworks.

The implications of this work extend beyond CYGNSS alone and are highly relevant for the growing number of commercial and research GNSS-R satellite missions. The error characterization and diagnostic tool developed here provides guidance for designing next-generation GNSS-R SM retrieval models. These insights also support future multi-constellation fusion efforts, which require consistent error characterizations across missions. The results presented here position CYGNSS SM V3.2 as a benchmark product for the GNSS-R community. Besides the empirical approaches, a future opportunity lies in polarimetric GNSS-R. Current GNSS-R systems operate with only one receiving polarization channel (Left-Hand Circularly Polarized). By incorporating an additional polarization channel, polarimetric spaceborne GNSS-R instruments can extract more information about vegetation and surface scattering mechanisms than conventional single-pol systems [71], [72]. This capability could open a pathway toward Level-2, trackwise, physically based SM retrievals with reduced ambiguity and enhanced geophysical interpretability.

VII. Conclusion

This study presents a comprehensive evaluation of the CYGNSS V3.2 SM product over its full seven-year record. We establish a direct connection between specific Level-0 and Level-1 calibration upgrades including dynamic EIRP correction, refined DDM noise-floor estimation, and temperature-dependent receiver compensation, and the resulting improvements in Level-3 SM retrieval accuracy and temporal stability. The improved L1 calibration yields measurable gains in SM accuracy, reduced long-term bias drift (including the correction of the post-2020 GPS Flex Power discontinuity), and enhanced consistency across the seven-year record. The improvements in SM retrieval are corroborated by SMAP cross-product comparison, in-situ SM validation, and the Triple Collocation method.

Spatial and temporal analyses reflect several fundamental environmental constraints on empirical GNSS-R SM retrieval. The CYGNSS SM retrieval error compared with SMAP increases as land cover heterogeneity increases, indicating representativeness limitations due to the scale mismatch between CYGNSS observations and the coarser reference datasets used for model training. The CYGNSS SM year-mean bias compared with SMAP increases faster in high water fraction area while it remains stable in low water fraction area, suggesting that the observed multi-year bias drift is consistent with inland-water contamination that is only partially mitigated by the existing static water mask. The CYGNSS retrieval bias and ubRMSD compared with SMAP and ISMN show correlation with VOD, reflecting that vegetation phenology generates strong seasonal variations in retrieval errors which empirical models trained under fixed surface conditions represent only implicitly. The model-stability diagnostics reveal characteristic regimes of reduced train-test stability in empirical GNSS-R SM models, driven by data sparsity, weak reflectivity–SM sensitivity, and limited SM dynamic range in certain environments. While CYGNSS V3.2 benefits from multi-year training and shows improved robustness, some of these limitations persist and reflect broader constraints shared across other current GNSS-R missions.

Looking forward, addressing the limitations identified in this study will require GNSS-R systems to more fully exploit their unique measurement capabilities. Dynamic inland water masks derived directly from GNSS-R observations may help mitigate water-related biases that the static optical water mask cannot capture, and provide a direct test of the dynamic water attribution proposed in Section IV G. Vegetation-aware or semi-empirical modeling approaches offer a pathway to account for seasonal changes in vegetation water content and biomass. Improved strategies for ensuring train-test stability are needed to enhance retrieval robustness across diverse environments. Finally, polarimetric GNSS-R represents a promising direction for developing more physically based soil-moisture retrievals, as the additional polarization channel provides additional sensitivity to vegetation structure and scattering mechanisms not available to current single-pol systems. Together, these advances can form the foundation for next-generation GNSS-R soil-moisture retrieval frameworks and future multi-constellation GNSS-R missions with robust improvements in performance.

Acknowledgment

The authors would like to thank the CYGNSS Science Team for supporting the CYGNSS L3 V3.2 SM product retrieval algorithm. This work was supported in part by the NASA Science Mission Directorate under Contract NNL13AQ00C with the University of Michigan.

References

[1] K. A. McColl, S. H. Alemohammad, R. Akbar, A. G. Konings, S. Yueh, and D. Entekhabi, “The global distribution and dynamics of surface soil moisture,” *Nat. Geosci.*, vol. 10, no. 2, pp. 100–104, Feb. 2017, doi: 10.1038/ngeo2868.

[2] N. Wanders, M. F. P. Bierkens, S. M. de Jong, A. de Roo, and D. Karssenberg, “The benefits of using remotely sensed soil moisture in parameter identification of large-scale hydrological models,” *Water Resour. Res.*, vol. 50, no. 8, pp. 6874–6891, 2014, doi: 10.1002/2013WR014639.

[3] M. Drusch, “Initializing numerical weather prediction models with satellite-derived surface soil moisture: Data

This work is licensed under a Creative Commons Attribution 4.0 License. For more information, see https://creativecommons.org/licenses/by/4.0/

This article has been accepted for publication in IEEE Journal of Selected Topics in Applied Earth Observations and Remote Sensing. This is the author's version which has not been fully edited and content may change prior to final publication. Citation information: DOI 10.1109/JSTARS.2026.3715093

assimilation experiments with ECMWF's Integrated Forecast System and the TMI soil moisture data set," *J. Geophys. Res. Atmospheres*, vol. 112, no. D3, 2007, doi: 10.1029/2006JD007478.

[4] R. J. Oglesby and D. J. Erickson, "Soil Moisture and the Persistence of North American Drought," Nov. 1989, Accessed: Jul. 31, 2025. [Online]. Available: https://journals.ametsoc.org/view/journals/clim/2/11/1520-0442_1989_002_1362_smatpo_2_0_co_2.xml

[5] J. Sheffield and E. F. Wood, "Global Trends and Variability in Soil Moisture and Drought Characteristics, 1950–2000, from Observation-Driven Simulations of the Terrestrial Hydrologic Cycle," Feb. 2008, doi: 10.1175/2007JCLI1822.1.

[6] L. Brocca *et al.*, "How much water is used for irrigation? A new approach exploiting coarse resolution satellite soil moisture products," *Int. J. Appl. Earth Obs. Geoinformation*, vol. 73, pp. 752–766, Dec. 2018, doi: 10.1016/j.jag.2018.08.023.

[7] M. T. Hallikainen, F. T. Ulaby, M. C. Dobson, M. A. El-rayes, and L. Wu, "Microwave Dielectric Behavior of Wet Soil-Part 1: Empirical Models and Experimental Observations," *IEEE Trans. Geosci. Remote Sens.*, vol. GE-23, no. 1, pp. 25–34, Jan. 1985, doi: 10.1109/TGRS.1985.289497.

[8] D. Entekhabi *et al.*, "The Soil Moisture Active Passive (SMAP) Mission," *Proc. IEEE*, vol. 98, no. 5, pp. 704–716, May 2010, doi: 10.1109/JPROC.2010.2043918.

[9] Y. H. Kerr *et al.*, "The SMOS Mission: New Tool for Monitoring Key Elements ofthe Global Water Cycle," *Proc. IEEE*, vol. 98, no. 5, pp. 666–687, May 2010, doi: 10.1109/JPROC.2010.2043032.

[10] A. Rosenqvist, M. Shimada, N. Ito, and M. Watanabe, "ALOS PALSAR: A Pathfinder Mission for Global-Scale Monitoring of the Environment," *IEEE Trans. Geosci. Remote Sens.*, vol. 45, no. 11, pp. 3307–3316, Nov. 2007, doi: 10.1109/TGRS.2007.901027.

[11] V. U. Zavorotny, S. Gleason, E. Cardellach, and A. Camps, "Tutorial on Remote Sensing Using GNSS Bistatic Radar of Opportunity," *IEEE Geosci. Remote Sens. Mag.*, vol. 2, no. 4, pp. 8–45, Dec. 2014, doi: 10.1109/MGRS.2014.2374220.

[12] S. Gleason *et al.*, "Detection and Processing of bistatically reflected GPS signals from low Earth orbit for the purpose of ocean remote sensing," *IEEE Trans. Geosci. Remote Sens.*, vol. 43, no. 6, pp. 1229–1241, Jun. 2005, doi: 10.1109/TGRS.2005.845643.

[13] M. Unwin, P. Jales, J. Tye, C. Gommenginger, G. Foti, and J. Rosello, "Spaceborne GNSS-Reflectometry on TechDemoSat-1: Early Mission Operations and Exploitation," *IEEE J. Sel. Top. Appl. Earth Obs. Remote Sens.*, vol. 9, no. 10, pp. 4525–4539, Oct. 2016, doi: 10.1109/JSTARS.2016.2603846.

[14] C. S. Ruf *et al.*, "A New Paradigm in Earth Environmental Monitoring with the CYGNSS Small Satellite Constellation," *Sci. Rep.*, vol. 8, no. 1, Art. no. 1, Jun. 2018, doi: 10.1038/s41598-018-27127-4.

[15] C. S. Ruf *et al.*, "New ocean winds satellite mission to probe hurricanes and tropical convection," *Bull. Am. Meteorol. Soc.*, vol. 97, no. 3, pp. 385–395, 2016.

[16] A. Camps *et al.*, "Sensitivity of GNSS-R spaceborne observations to soil moisture and vegetation," *IEEE J. Sel. Top. Appl. Earth Obs. Remote Sens.*, vol. 9, no. 10, pp. 4730–4742, 2016.

[17] C. C. Chew and E. E. Small, "Soil Moisture Sensing Using Spaceborne GNSS Reflections: Comparison of CYGNSS Reflectivity to SMAP Soil Moisture," *Geophys. Res. Lett.*, vol. 45, no. 9, pp. 4049–4057, 2018, doi: 10.1029/2018GL077905.

[18] H. Kim and V. Lakshmi, "Use of Cyclone Global Navigation Satellite System (CyGNSS) Observations for Estimation of Soil Moisture," *Geophys. Res. Lett.*, vol. 45, no. 16, pp. 8272–8282, 2018, doi: 10.1029/2018GL078923.

[19] C. Ruf and S. Gleason, "Spaceborne GNSS-R Bistatic Radar Remote Sensing, CYGNSS, and Future Missions," *Proc. IEEE*, pp. 1–19, 2025, doi: 10.1109/JPROC.2025.3583997.

[20] C. Chew and E. Small, "Description of the UCAR/CU Soil Moisture Product," *Remote Sens.*, vol. 12, no. 10, Art. no. 10, Jan. 2020, doi: 10.3390/rs12101558.

[21] M. M. Al-Khaldi, J. T. Johnson, A. J. O'Brien, A. Balenzano, and F. Mattia, "Time-Series Retrieval of Soil Moisture Using CYGNSS," *IEEE Trans. Geosci. Remote Sens.*, vol. 57, no. 7, pp. 4322–4331, Jul. 2019, doi: 10.1109/TGRS.2018.2890646.

[22] M. P. Clarizia, N. Pierdicca, F. Costantini, and N. Floury, "Analysis of CYGNSS Data for Soil Moisture Retrieval," *IEEE J. Sel. Top. Appl. Earth Obs. Remote Sens.*, vol. 12, no. 7, pp. 2227–2235, Jul. 2019, doi: 10.1109/JSTARS.2019.2895510.

[23] P. T. Setti and S. Tabibi, "Comprehensive Analysis of CYGNSS GNSS-R data for Enhanced Soil Moisture Retrieval," *IEEE J. Sel. Top. Appl. Earth Obs. Remote Sens.*, pp. 1–18, 2024, doi: 10.1109/JSTARS.2024.3498069.

[24] A. Melebari, J. D. Campbell, E. Hodges, and M. Moghaddam, "Sensitivity Analysis OF GNSS-R Delay Doppler Maps to Soil Moisture and Vegetation Using a Physics-Based Model," in *IGARSS 2024-2024 IEEE International Geoscience and Remote Sensing Symposium*, IEEE, 2024, pp. 823–826. Accessed: Jul. 31, 2025. [Online]. Available: https://ieeexplore.ieee.org/abstract/document/10641646/

[25] S. H. Yueh, R. Shah, M. J. Chaubell, A. Hayashi, X. Xu, and A. Colliander, "A Semiempirical Modeling of Soil Moisture, Vegetation, and Surface Roughness Impact on CYGNSS Reflectometry Data," *IEEE Trans. Geosci. Remote Sens.*, vol. 60, pp. 1–17, 2022, doi: 10.1109/TGRS.2020.3035989.

[26] O. Eroglu, M. Kurum, D. Boyd, and A. C. Gurbuz, "High Spatio-Temporal Resolution CYGNSS Soil Moisture Estimates Using Artificial Neural Networks," *Remote Sens.*, vol. 11, no. 19, Art. no. 19, Jan. 2019, doi: 10.3390/rs11192272.

This work is licensed under a Creative Commons Attribution 4.0 License. For more information, see https://creativecommons.org/licenses/by/4.0/

This article has been accepted for publication in IEEE Journal of Selected Topics in Applied Earth Observations and Remote Sensing. This is the author's version which has not been fully edited and content may change prior to final publication. Citation information: DOI 10.1109/JSTARS.2026.3715093

[27] M. M. Nabi, V. Senyurek, F. Lei, M. Kurum, and A. C. Gurbuz, "Quasi-Global Assessment of Deep Learning-Based CYGNSS Soil Moisture Retrieval," *IEEE J. Sel. Top. Appl. Earth Obs. Remote Sens.*, vol. 16, pp. 5629–5644, 2023, doi: 10.1109/JSTARS.2023.3287591.

[28] M. M. Nabi, V. Senyurek, A. C. Gurbuz, and M. Kurum, "Deep Learning-Based Soil Moisture Retrieval in CONUS Using CYGNSS Delay–Doppler Maps," *IEEE J. Sel. Top. Appl. Earth Obs. Remote Sens.*, vol. 15, pp. 6867–6881, 2022, doi: 10.1109/JSTARS.2022.3196658.

[29] M. M. Al-Khaldi *et al.*, "An Analysis of a Commercial GNSS-R Soil Moisture Dataset," *IEEE J. Sel. Top. Appl. Earth Obs. Remote Sens.*, vol. 17, pp. 15480–15493, 2024, doi: 10.1109/JSTARS.2024.3449773.

[30] M. Roberts, I. Colwell, C. Chew, D. Masters, and K. Nordstrom, "The Muon Space GNSS-R Surface Soil Moisture Product," Nov. 26, 2024, *arXiv*: arXiv:2412.00072. doi: 10.48550/arXiv.2412.00072.

[31] C. Yin *et al.*, "Soil Moisture Retrieval from Multi-GNSS Reflectometry on FY-3E GNOS-II by Land Cover Classification," *Remote Sens.*, vol. 15, no. 4, p. 1097, Jan. 2023, doi: 10.3390/rs15041097.

[32] Q. Wang, C. Lu, Y. Zheng, Z. Wang, J. Li, and Y. Tan, "In-situ and triple collocation-based evaluations of Tianmu-1 global soil moisture products," *Remote Sens. Environ.*, vol. 328, p. 114892, Oct. 2025, doi: 10.1016/j.rse.2025.114892.

[33] T. Wang *et al.*, "Dynamic Calibration of GPS Effective Isotropic Radiated Power for GNSS-Reflectometry Earth Remote Sensing," *IEEE Trans. Geosci. Remote Sens.*, vol. 60, pp. 1–12, 2022, doi: 10.1109/TGRS.2021.3070238.

[34] S. Gleason, M. M. Al-Khaldi, C. S. Ruf, D. S. McKague, T. Wang, and A. Russel, "Characterizing and Mitigating Digital Sampling Effects on the CYGNSS Level 1 Calibration," *IEEE Trans. Geosci. Remote Sens.*, vol. 60, pp. 1–12, 2022, doi: 10.1109/TGRS.2021.3120026.

[35] M. M. Al-Khaldi *et al.*, "Quantifying and Correcting Thermally Driven Oscillations in CYGNSS Real-Time GPS Effective Isotropic Radiated Power," *IEEE Trans. Geosci. Remote Sens.*, pp. 1–1, 2025, doi: 10.1109/TGRS.2025.3538681.

[36] E. Hodges *et al.*, "A Merged CYGNSS Soil Moisture Product Using a Minimum Variance Estimator," *IEEE Trans. Geosci. Remote Sens.*, vol. 63, pp. 1–15, 2025, doi: 10.1109/TGRS.2025.3597532.

[37] C. Ruf *et al.*, *CYGNSS Handbook*. Michigan Publishing Services, 2022. doi: 10.3998/mpub.12741920.

[38] A. Camps, "Spatial Resolution in GNSS-R Under Coherent Scattering," *IEEE Geosci. Remote Sens. Lett.*, vol. 17, no. 1, pp. 32–36, Jan. 2020, doi: 10.1109/LGRS.2019.2916164.

[39] V. L. Mironov, L. G. Kosolapova, and S. V. Fomin, "Physically and Mineralogically Based Spectroscopic Dielectric Model for Moist Soils," *IEEE Trans. Geosci. Remote Sens.*, vol. 47, no. 7, pp. 2059–2070, Jul. 2009, doi: 10.1109/TGRS.2008.2011631.

[40] H. H. Nguyen *et al.*, "From theory to hydrological practice: Leveraging CYGNSS data over seven years for advanced soil moisture monitoring," *Remote Sens. Environ.*, vol. 316, p. 114509, Jan. 2025, doi: 10.1016/j.rse.2024.114509.

[41] W. Yang, F. Guo, X. Zhang, Y. Zhu, Z. Li, and Z. Zhang, "First quasi-global soil moisture retrieval using Fengyun-3 GNSS-R constellation observations," *Remote Sens. Environ.*, vol. 321, p. 114653, May 2025, doi: 10.1016/j.rse.2025.114653.

[42] D. Bai, C. Chew, and E. Small, "Algorithm Theoretical Basis Document Level 3 Soil Moisture," NASA / Jet Propulsion Laboratory (JPL), 148–0413, 2025. Accessed: Nov. 29, 2025. [Online]. Available: https://archive.podaac.earthdata.nasa.gov/podaac-ops-cumulus-docs/cygnss/open/L3/docs/148-0413_ATBD_L3_Soil_Moisture_Rev1.pdf

[43] P. E. O'Neill *et al.*, "SMAP Enhanced L3 Radiometer Global and Polar Grid Daily 9 km EASE-Grid Soil Moisture. (SPL3SMP_E, Version 6)." NASA National Snow and Ice Data Center Distributed Active Archive Center, Boulder, Colorado USA, 2023. doi: 10.5067/M20OXIZHY3RJ.

[44] P. E. O'Neill, S. Chan, E. Njoku, T. Jackson, R. Bindlish, and J. Chaubell, "SMAP L3 Radiometer Global Daily 36 km EASE-Grid Soil Moisture. (SPL3SMP, Version 8)." NASA National Snow and Ice Data Center Distributed Active Archive Center, Boulder, Colorado USA., 2021. doi: 10.5067/OMHVSRGFX38O.

[45] W. Dorigo *et al.*, "ESA Soil Moisture Climate Change Initiative (Soil_Moisture_cci): ACTIVE product, Version 09.2." NERC EDS Centre for Environmental Data Analysis, p. 12124 Files, 7860905106 B, 2025. doi: 10.5285/2600F842CFEB481BB21F032A5741C353.

[46] W. Dorigo *et al.*, "The International Soil Moisture Network: serving Earth system science for over a decade," *Hydrol. Earth Syst. Sci.*, vol. 25, no. 11, pp. 5749–5804, Nov. 2021, doi: 10.5194/hess-25-5749-2021.

[47] D. R. Cook, "Soil Temperature and Moisture Profile (STAMP) System Handbook," ARM Climate Research Facility, Pacific Northwest National Laboratory, Richland, WA, DOE/SC-ARM-TR--186, Nov. 2016. doi: 10.2172/1332724.

[48] A. B. Smith *et al.*, "The Murrumbidgee soil moisture monitoring network data set," *Water Resour. Res.*, vol. 48, no. 7, 2012, doi: 10.1029/2012WR011976.

[49] G. L. Schaefer, M. H. Cosh, and T. J. Jackson, "The USDA Natural Resources Conservation Service Soil Climate Analysis Network (SCAN)," Dec. 2007, doi: 10.1175/2007JTECHA930.1.

[50] G. H. Leavesley *et al.*, "A Modeling Framework for Improved Agricultural Water Supply Forecasting," presented at the AGU Fall Meeting Abstracts, Dec. 2008, pp. C21A-0497. Accessed: Aug. 01, 2025. [Online]. Available: https://ui.adsabs.harvard.edu/abs/2008AGUFM.C21A0497L

[51] M. Moghaddam *et al.*, "A Wireless Soil Moisture Smart Sensor Web Using Physics-Based Optimal Control: Concept and Initial Demonstrations," *IEEE J. Sel. Top. Appl. Earth Obs. Remote Sens.*, vol. 3, no. 4, pp. 522–535, Dec. 2010, doi: 10.1109/JSTARS.2010.2052918.

This work is licensed under a Creative Commons Attribution 4.0 License. For more information, see https://creativecommons.org/licenses/by/4.0/

This article has been accepted for publication in IEEE Journal of Selected Topics in Applied Earth Observations and Remote Sensing. This is the author's version which has not been fully edited and content may change prior to final publication. Citation information: DOI 10.1109/JSTARS.2026.3715093

[52] J. E. Bell *et al.*, "U.S. Climate Reference Network Soil Moisture and Temperature Observations," Jun. 2013, doi: 10.1175/JHM-D-12-0146.1.

[53] N. van de Giesen, R. Hut, and J. Selker, "The Trans-African Hydro-Meteorological Observatory (TAHMO)," *WIREs Water*, vol. 1, no. 4, pp. 341–348, 2014, doi: 10.1002/wat2.1034.

[54] T. G. Caldwell *et al.*, "The Texas Soil Observation Network:A Comprehensive Soil Moisture Dataset for Remote Sensing and Land Surface Model Validation," *Vadose Zone J.*, vol. 18, no. 1, p. 190034, 2019, doi: 10.2136/vzj2019.04.0034.

[55] M. Friedl and D. Sulla-Menashe, "MODIS/Terra+Aqua Land Cover Type Yearly L3 Global 0.05Deg CMG V061." NASA Land Processes Distributed Active Archive Center, Sioux Falls, South Dakota, USA, 2022. doi: 10.5067/MODIS/MCD12C1.061.

[56] D. Entekhabi, R. H. Reichle, R. D. Koster, and W. T. Crow, "Performance Metrics for Soil Moisture Retrievals and Application Requirements," Jun. 2010, doi: 10.1175/2010JHM1223.1.

[57] A. Stoffelen, "Toward the true near-surface wind speed: Error modeling and calibration using triple collocation," *J. Geophys. Res. Oceans*, vol. 103, no. C4, pp. 7755–7766, 1998, doi: 10.1029/97JC03180.

[58] K. A. McColl, J. Vogelzang, A. G. Konings, D. Entekhabi, M. Piles, and A. Stoffelen, "Extended triple collocation: Estimating errors and correlation coefficients with respect to an unknown target," *Geophys. Res. Lett.*, vol. 41, no. 17, pp. 6229–6236, 2014, doi: 10.1002/2014GL061322.

[59] A. Gruber, C.-H. Su, W. T. Crow, S. Zwieback, W. A. Dorigo, and W. Wagner, "Estimating error cross-correlations in soil moisture data sets using extended collocation analysis," *J. Geophys. Res. Atmospheres*, vol. 121, no. 3, pp. 1208–1219, 2016, doi: 10.1002/2015JD024027.

[60] F. Chen *et al.*, "Global-scale evaluation of SMAP, SMOS and ASCAT soil moisture products using triple collocation," *Remote Sens. Environ.*, vol. 214, pp. 1–13, Sep. 2018, doi: 10.1016/j.rse.2018.05.008.

[61] R. Balasubramaniam and C. Ruf, "The Impact on Triple/N-Way Collocation-Based Validation of Remote Sensing Products Due to Non-Ideal Error Statistics," *Remote Sens.*, vol. 17, no. 22, p. 3751, Jan. 2025, doi: 10.3390/rs17223751.

[62] S. K. Chan *et al.*, "Development and assessment of the SMAP enhanced passive soil moisture product," *Remote Sens. Environ.*, vol. 204, pp. 931–941, Jan. 2018, doi: 10.1016/j.rse.2017.08.025.

[63] C. D. Bussy-Virat, C. S. Ruf, and A. J. Ridley, "Relationship Between Temporal and Spatial Resolution for a Constellation of GNSS-R Satellites," *IEEE J. Sel. Top. Appl. Earth Obs. Remote Sens.*, vol. 12, no. 1, pp. 16–25, Jan. 2019, doi: 10.1109/JSTARS.2018.2833426.

[64] C. Ruf *et al.*, "Characterization of CYGNSS Ocean Surface Wind Speed Products," *Remote Sens.*, vol. 16, no. 22, Art. no. 22, Jan. 2024, doi: 10.3390/rs16224341.

[65] C. Chew and E. Small, "UCAR/CU CYGNSS Soil Moisture Product User Guide." 2022.

[66] "SMAP Handbook." 2017.

[67] H. Carreno-Luengo, C. S. Ruf, S. Gleason, and A. Russel, "Detection of inland water bodies under dense biomass by CYGNSS," *Remote Sens. Environ.*, vol. 301, p. 113896, Feb. 2024, doi: 10.1016/j.rse.2023.113896.

[68] T. Pu, C. Gerlein-Safdi, Y. Xiong, M. Li, E. A. Kort, and A. A. Bloom, "Berkeley-RWAWC: A New CYGNSS-Based Watermask Unveils Unique Observations of Seasonal Dynamics in the Tropics," *Water Resour. Res.*, vol. 60, no. 7, p. e2024WR037060, 2024, doi: 10.1029/2024WR037060.

[69] C. Jones, Y. Mu, L. M. V. Carvalho, and Q. Ding, "The South America Low-Level Jet: form, variability and large-scale forcings," *Npj Clim. Atmospheric Sci.*, vol. 6, no. 1, p. 175, Oct. 2023, doi: 10.1038/s41612-023-00501-4.

[70] T. J. Jackson and T. J. Schmugge, "Vegetation effects on the microwave emission of soils," *Remote Sens. Environ.*, vol. 36, no. 3, pp. 203–212, Jun. 1991, doi: 10.1016/0034-4257(91)90057-D.

[71] D. Bai, C. S. Ruf, and D. Moller, "Calibration of the Polarimetric GNSS-R Sensor in the Rongowai Mission," *IEEE Trans. Geosci. Remote Sens.*, vol. 63, pp. 1–18, 2025, doi: 10.1109/TGRS.2025.3558131.

[72] N. Rodriguez-Alvarez, J. F. Munoz-Martin, X. Bosch-Lluis, K. Oudrhiri, D. Entekhabi, and A. Colliander, "The first polarimetric GNSS-Reflectometer instrument in space improves the SMAP mission's sensitivity over densely vegetated areas," *Sci. Rep.*, vol. 13, no. 1, p. 3722, Mar. 2023, doi: 10.1038/s41598-023-30805-7.



Dinan Bai (Member, IEEE) received his B.S. degree in Electrical and Computer Engineering with Honors Research Distinction from the Ohio State University, Columbus, OH, USA, in 2022, and the M.S. degree in Electrical and Computer Engineering from University of Michigan, Ann Arbor, USA, in 2024, where he is currently pursuing the Ph.D. degree with the Department of Climate and Space Science and Engineering.

Since 2022, he has been a Graduate Research Assistant with the Remote Sensing Group, Department of Climate and Space Science and Engineering, University of Michigan. His research interests include applied electromagnetics, Microwave Remote Sensing system design, calibration, and application.



Anthony Russel received the B.S. degree in computer science engineering from Michigan State University, East Lansing, MI, USA, in 2014.

He is a software Engineer at Muon Space since Aug 2025. He has worked previously as a member of the engineering staff with the Space Physics Research Laboratory, College of Engineering, University of Michigan, Ann Arbor, MI, USA. His primary engineering activities involve algorithm development and large-scale data

This work is licensed under a Creative Commons Attribution 4.0 License. For more information, see https://creativecommons.org/licenses/by/4.0/

This article has been accepted for publication in IEEE Journal of Selected Topics in Applied Earth Observations and Remote Sensing. This is the author's version which has not been fully e
content may change prior to final publication. Citation information: DOI 10.1109/JSTARS.2026.3715093

processing as a Member of the Science Operations Center for the CYGNSS Mission.



Christopher S. Ruf (Life Fellow, IEEE), received the B.A. degree in physics from Reed College, Portland, OR, USA, in 1982, and the Ph.D. degree in electrical and computer engineering from the University of Massachusetts, Amherst, MA, USA, in 1987.

He is the Frederick Bartman Collegiate Professor of climate and space science with the University of Michigan and Principal Investigator of the NASA Cyclone Global Navigation Satellite System Mission. He has worked previously at Intel Corporation, Hughes Space and Communication, the NASA Jet Propulsion Laboratory, and Penn State University. His research interests include GNSS-R remote sensing, microwave radiometry, atmosphere and ocean geophysical retrieval algorithm development, and sensor technology development.

Dr. Ruf is a member of the National Academy of Engineering, , Fellow of the American Meteorological Society, Vice Chair of Commission F of the Union Radio Scientifique International, and member of the American Geophysical Union. He was a recipient of the 1997 IEEE TGRS Best Paper Award, the 1999 IEEE Resnik Technical Field Award, the 2006 IGARSS Best Paper Award, the 2014 IEEE GRSS Outstanding Service Award, the 2017 AIAA SmallSat Mission of the Year Award, and the 2020 University of Michigan Distinguished Faculty Achievement Award. He is a former Editor-in-Chief of the IEEE TRANSACTIONS ON GEOSCIENCE AND REMOTE SENSING and has served on the editorial boards of Radio Science, the Journal of Atmospheric and Oceanic Technology, and Nature Scientific Reports.

This work is licensed under a Creative Commons Attribution 4.0 License. For more information, see https://creativecommons.org/licenses/by/4.0/